LETTER

doi:10.1038/nature14234

N^6-methyladenosine-dependent RNA structural switches regulate RNA–protein interactions

Nian Liu[1], Qing Dai[1], Guanqun Zheng[2], Chuan He[1,2,3,4], Marc Parisien[2]† & Tao Pan[2,3]

RNA-binding proteins control many aspects of cellular biology through binding single-stranded RNA binding motifs (RBMs)[1–3]. However, RBMs can be buried within their local RNA structures[4–7], thus inhibiting RNA–protein interactions. N^6-methyladenosine (m^6A), the most abundant and dynamic internal modification in eukaryotic messenger RNA[8–19], can be selectively recognized by the YTHDF2 protein to affect the stability of cytoplasmic mRNAs[15], but how m^6A achieves its wide-ranging physiological role needs further exploration. Here we show in human cells that m^6A controls the RNA-structure-dependent accessibility of RBMs to affect RNA–protein interactions for biological regulation; we term this mechanism 'the m^6A-switch'. We found that m^6A alters the local structure in mRNA and long non-coding RNA (lncRNA) to facilitate binding of heterogeneous nuclear ribonucleoprotein C (HNRNPC), an abundant nuclear RNA-binding protein responsible for pre-mRNA processing[20–24]. Combining photoactivatable-ribonucleoside-enhanced crosslinking and immunoprecipitation (PAR-CLIP) and anti-m^6A immunoprecipitation (MeRIP) approaches enabled us to identify 39,060 m^6A-switches among HNRNPC-binding sites; and global m^6A reduction decreased HNRNPC binding at 2,798 high-confidence m^6A-switches. We determined that these m^6A-switch-regulated HNRNPC-binding activities affect the abundance as well as alternative splicing of target mRNAs, demonstrating the regulatory role of m^6A-switches on gene expression and RNA maturation. Our results illustrate how RNA-binding proteins gain regulated access to their RBMs through m^6A-dependent RNA structural remodelling, and provide a new direction for investigating RNA-modification-coded cellular biology.

Post-transcriptional m^6A RNA modification is indispensable for cell viability and development, yet its functional mechanisms are still poorly understood[8–19]. We recently identified one m^6A site in a hairpin-stem

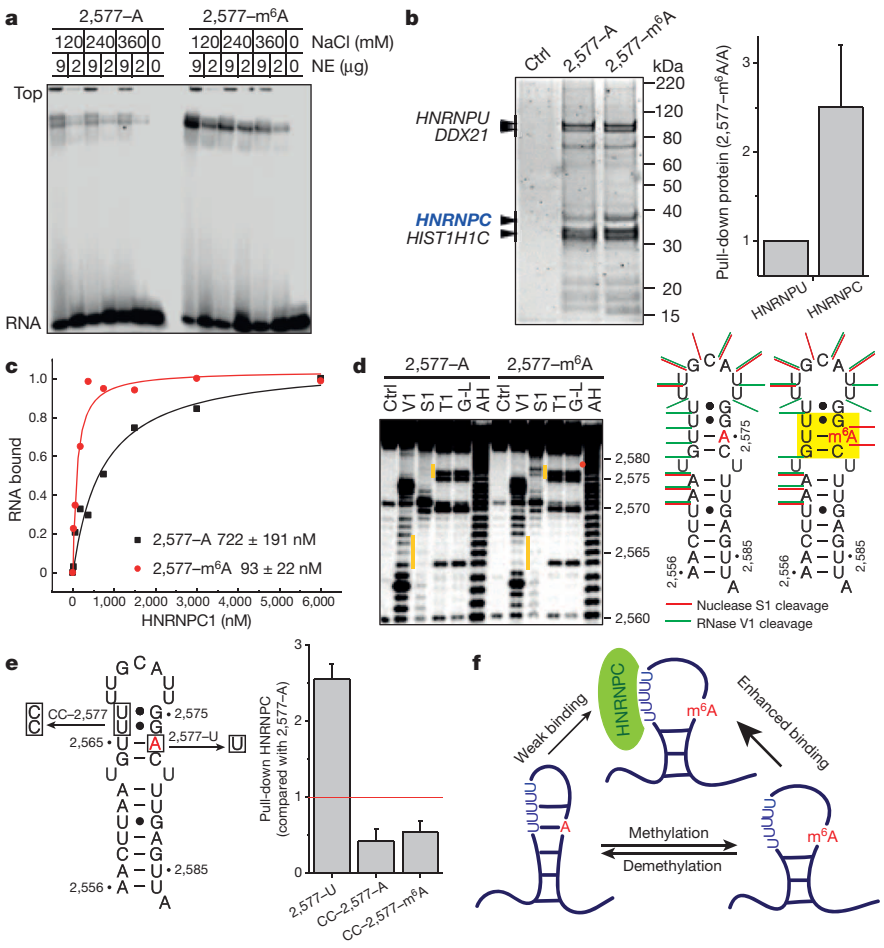

Figure 1 | m^6A alters RNA structure to enhance HNRNPC binding. **a**, m^6A increases binding with nuclear proteins. NE, nuclear extract. **b**, RNA pull down showing that HNRNPC preferably binds methylated RNA. Data are mean ± standard deviation (s.d.); $n = 4$, biological replicates. Ctrl, control. **c**, Filter binding showing that m^6A increases HNRNPC1 binding with respective apparent dissociation constants (K_d) indicated at bottom right. Data are mean ± s.d.; $n = 3$, technical replicates. **d**, RNA structural probing showing that m^6A disrupts local RNA structure, highlighted in yellow. AH, alkaline hydrolysis; Ctrl, no nuclease added; G-L, G-ladder; S1, nuclease S1 digestion; T1, RNase T1 digestion; V1, RNase V1 digestion. The orange bars mark the structurally altered RNA regions in the presence of m^6A (red dot). **e**, RNA pull down with mutated oligonucleotides. Data are mean ± s.d.; $n = 3$, technical replicates. **f**, Illustration of the m^6A-switch model.

[1]Department of Chemistry, The University of Chicago, Chicago, Illinois 60637, USA. [2]Department of Biochemistry and Molecular Biology, The University of Chicago, Chicago, Illinois 60637, USA. [3]Institute for Biophysical Dynamics, The University of Chicago, Chicago, Illinois 60637, USA. [4]Howard Hughes Medical Institute, The University of Chicago, Chicago, Illinois 60637, USA. †Present address: Faculty of Dentistry, McGill University, Montreal, Quebec H3A 0G1, Canada.

on the human lncRNA metastasis-associated lung adenocarcinoma transcript (*MALAT1*)[25] (Extended Data Fig. 1a). A native gel-shift assay indicated that this m^{6}A residue increases the interaction of the RNA hairpin with proteins in the HeLa nuclear extract (Fig. 1a). RNA pull-down assays identified HNRNPC as the protein component of the nuclear extract that binds more strongly with the m^{6}A-modified hairpin than the unmodified hairpin (Fig. 1b and Extended Data Fig. 1b, c). The m^{6}A-enhanced interaction with the hairpins was validated qualitatively by ultraviolet crosslinking and quantitatively (~8-fold increase) by filter binding using recombinant HNRNPC1 protein (Fig. 1c and Extended Data Fig. 1d).

The HNRNPC protein belongs to the large family of ubiquitously expressed heterogeneous nuclear ribonucleoproteins that bind nascent RNA transcripts to affect pre-mRNA stability, splicing, export and translation[20–24]. HNRNPC preferably binds single-stranded U-tracts (five or more contiguous uridines)[20,23,24,26,27]. In the *MALAT1* hairpin, HNRNPC binds a U_5-tract that is half buried in the hairpin-stem opposing the 2,577–A/m^{6}A site (Extended Data Fig. 1a, e).

Since m^{6}A residues within RNA stems can destabilize the thermostability of model RNA duplexes[28], we hypothesized that the 2,577–m^{6}A residue destabilizes this *MALAT1* hairpin-stem to make its opposing U-tract more single-stranded or accessible, thus enhancing its interaction with HNRNPC. We performed several experiments to validate this hypothesis. First, according to the RNA structural probing assays, the m^{6}A-modified hairpin showed significantly increased nuclease S1 digestion (single-strand specific) at the GAC (A = m^{6}A) motif, as well as markedly decreased RNase V1 digestion (double-strand/stacking specific) at the U-tract opposing the GAC motif (Fig. 1d). The m^{6}A residue markedly destabilized the stacking properties of the region centred around the U residue that pairs with 2,577–A/m^{6}A (Extended Data Fig. 1f, g), which was also supported by the increased reactivity between CMCT and the U-tract bases in the presence of m^{6}A (Extended Data Fig. 1h). Second, the 2,577–A-to-U mutation increased the HNRNPC pull-down amount from the nuclear extract, whereas U-to-C mutations in the U-tract significantly reduced the HNRNPC pull-down amount regardless of m^{6}A modification (Fig. 1e). Third, the 2,577–A-to-U mutation increased the accessibility of the U-tract and enhanced HNRNPC binding by ~4-fold (Extended Data Fig. 2a–c). Binding results with four other mutated A/m^{6}A oligonucleotides also supported the U-tract, with increased accessibility alone being sufficient to enhance HNRNPC binding (Extended Data Fig. 2d). Fourth, RNA terminal truncation followed by HNRNPC binding identified two pairs of truncated hairpins with highly accessible U-tracts, which improved HNRNPC binding significantly but independent of the m^{6}A modification (Extended Data Fig. 2e–i). All these results confirmed that m^{6}A modification can alter its local RNA structure and enhance the accessibility of its base-paired

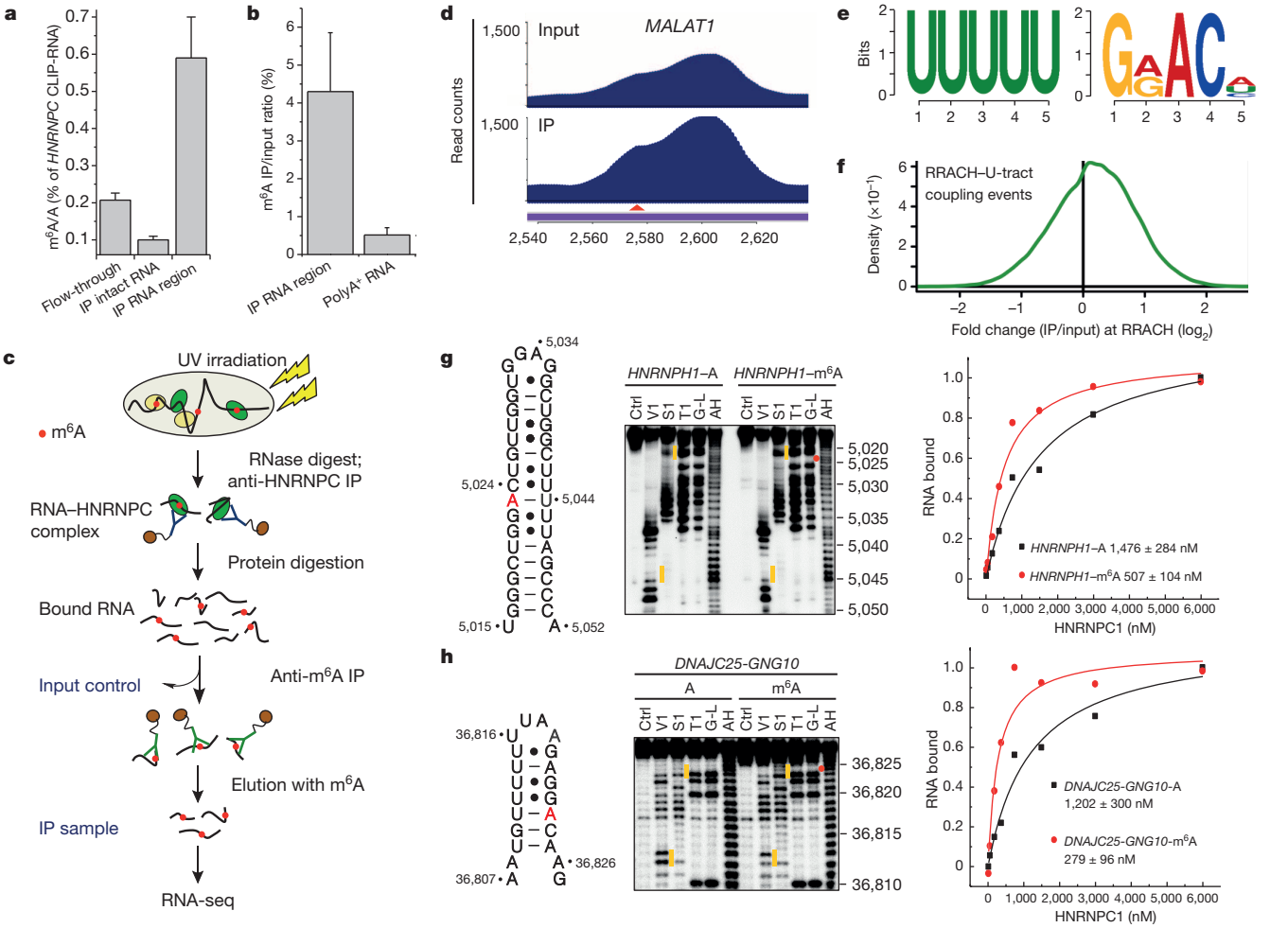

Figure 2 | PAR-CLIP–MeRIP identifies m^{6}A-switches transcriptome wide. **a**, CLIP-2dTLC showing the m^{6}A enrichment in HNRNPC-bound RNA regions. Data are mean ± s.d.; $n = 3$, biological replicates. IP, immunoprecipitation. **b**, HNRNPC-bound RNA regions had higher anti-m^{6}A pull-down yield than polyA$^+$ RNA. Data are mean ± s.d.; $n = 3$, biological replicates. **c**, Illustration of the PAR-CLIP–MeRIP protocol. UV, ultraviolet. **d**, PAR-CLIP–MeRIP identified an m^{6}A residue around the *MALAT1* 2,577 site. **e**, Binding motifs identified with PAR-CLIP–MeRIP peaks. **f**, Density plot showing the positive enrichment at RRACH sites. **g**, **h**, Validation of two m^{6}A-switches by S1/V1 structural probing and filter binding. Data are mean ± s.d.; $n = 4$, technical replicates. Annotation is the same as in Fig. 1c, d.

residues or nearby regions to modulate protein binding (Fig. 1f). We term this mechanism that regulates RNA–protein interactions through m^{6}A-dependent RNA structural remodelling 'the m^{6}A-switch'.

We performed two experiments to determine the global effect of m^{6}A-switches on HNRNPC binding. First, *in vivo* crosslinking followed by immunoprecipitation and two-dimensional thin-layer chromatography (CLIP-2dTLC) showed that the m^{6}A/A ratio of the HNRNPC-bound RNA regions had a ~6-fold higher m^{6}A level than the HNRNPC-bound intact RNA, and a ~3-fold higher m^{6}A level than the flow-through RNA (Fig. 2a and Extended Data Fig. 3a). Second, the HNRNPC-bound RNA regions had much higher anti-m^{6}A pull-down yield (4.3%) than the polyA$^+$ RNA samples (0.5%) using the previously established m^{6}A antibody[13,14] (Fig. 2b). These results indicate a widespread presence of m^{6}A residues in the vicinity of HNRNPC-binding sites.

To map the m^{6}A sites around HNRNPC-binding sites, we performed PAR-CLIP[29] to isolate all HNRNPC-bound RNA regions (input control sample) followed by MeRIP[13,14] to enrich m^{6}A-containing HNRNPC-bound RNA regions (IP sample). Both the input control and IP samples from two biological replicates were sent for RNA sequencing (RNA-seq) (Fig. 2c and Extended Data Fig. 3b, c). This approach, termed PAR-CLIP–MeRIP, identified transcriptome-wide the m^{6}A-proximal HNRNPC-binding site, such as the enriched peak around the *MALAT1* 2,577 site (Fig. 2d). Remarkably, HNRNPC PAR-CLIP–MeRIP peaks harboured two consensus motifs, the HNRNPC RBM (U-tracts) and the m^{6}A consensus motif GRACH (a subset of RRACH[13,14]) (Fig. 2e). Both motifs were located mostly within 50 residues, suggesting transcriptome-wide RRACH–U-tract coupling events within the HNRNPC-binding sites (Extended Data Fig. 4a, b). About 62% of all RRACH–U-tract coupling events within HNRNPC-binding sites are enriched at the RRACH motif (Fig. 2f). Our PAR-CLIP–MeRIP approach identified a total of 39,060 HNRNPC m^{6}A-switches that corresponded to m^{6}A-modified RRACH–U-tract coupling events at a false discovery rate (FDR) ≤ 5% (Extended Data Fig. 4c). These switches account for ~7% of 592,477 HNRNPC-binding sites identified by PAR-CLIP. The majority (87%) of m^{6}A-switches occur within introns (Extended Data Fig. 4d, e), consistent with the literature that HNRNPC is nuclear localized and primarily binds nascent transcripts[20,23]. We validated two intronic m^{6}A-switches in hairpin structures in which m^{6}A residues increase the U-tract accessibility and enhance HNRNPC binding by ~3–4 fold (Fig. 2g, h and Extended Data Fig. 5).

To assess the effect of global m^{6}A reduction on RNA–HNRNPC interactions, we performed HNRNPC PAR-CLIP experiments in *METTL3* and *METTL14* knockdown cells (Extended Data Fig. 6a). We identified 16,582 coupling events with decreased U-tract–HNRNPC interactions upon *METTL3* and *METTL14* knockdown (*METTL3/L14* knockdown) (Fig. 3a and Extended Data Fig. 6b, c). In total, 2,798 m^{6}A-switches identified by PAR-CLIP–MeRIP experiments showed decreased HNRNPC binding upon *METTL3/L14* knockdown (Fig. 3b) and this number is probably an underestimate due to the fact that *METTL3/L14* knockdown reduces the global m^{6}A level by only ~30–40% (refs 11, 12). These

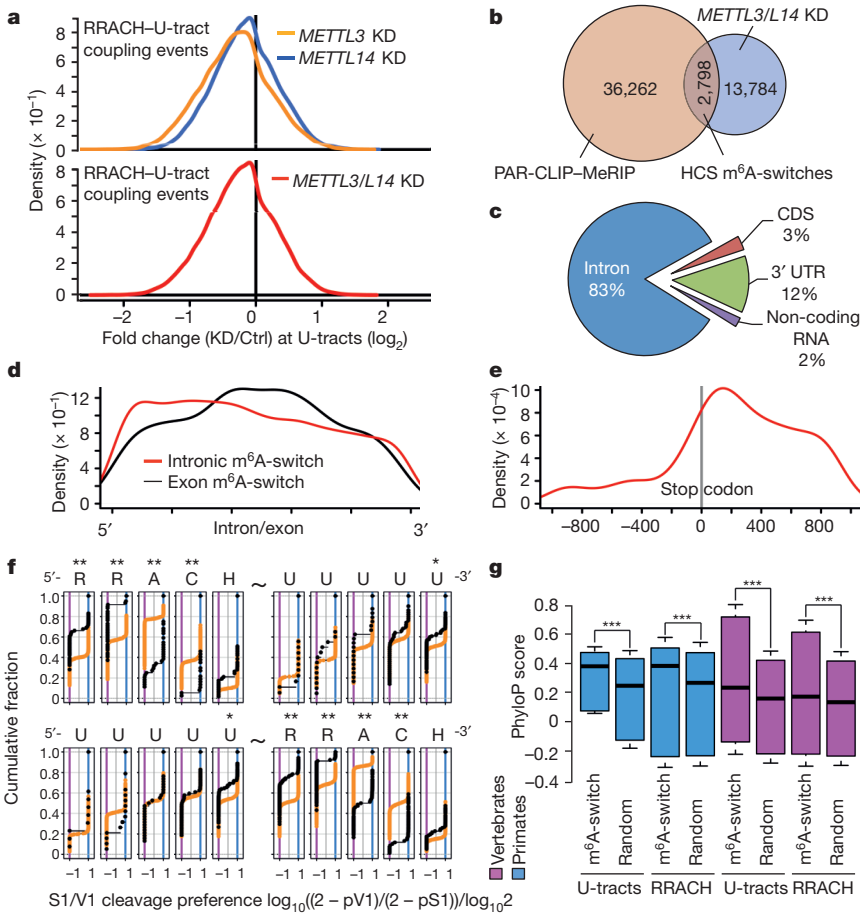

Figure 3 | Global m^{6}A reduction decreases HNRNPC binding at m^{6}A-switches. **a**, Density plot showing negative enrichment at the U-tracts. KD, knockdown. **b**, Identification of high-confidence (HCS) m^{6}A-switches. **c**, Regional distribution of high-confidence m^{6}A-switches. CDS, coding sequence. **d**, Density plot showing m^{6}A-switch distribution relative to exon/intron boundaries. **e**, m^{6}A-switches in coding RNA were enriched in the 3′ UTR and near the stop codon. **f**, Cumulative distribution of HCS m^{6}A-switches (black) and control (orange) regarding the S1/V1 cleavage preference (data from ref. 4) at U-tracts and RRACH motif. U-tract can be 3′ (top) or 5′ (bottom) of the RRACH motif. *$P < 0.05$, **$P < 10^{-4}$, Kolmogorov–Smirnov test. **g**, Phylogenetic conservation of high-confidence m^{6}A-switches among primates and vertebrates. ***$P < 10^{-16}$, Mann–Whitney–Wilcoxon test.

sites composed the high-confidence m^{6}A-switches that were used for subsequent analysis.

High-confidence m^{6}A-switches are enriched in the introns of coding and non-coding RNAs (Fig. 3c and Extended Data Fig. 6d). Exonic m^{6}A-switches are enriched at the middle of exons whereas intronic m^{6}A-switches are slightly enriched near the 5′ end (Fig. 3d). m^{6}A-switches within coding RNAs tend to locate at very long exons (Extended Data Fig. 6e) and are enriched near the stop codon and in the 3′ untranslated region (UTR) (Fig. 3e), consistent with the known topology of the human m^{6}A methylome in mRNAs[13,14]. Transcriptome-wide RNA structural mapping[4–7] on high-confidence m^{6}A-switches yielded consistent structural patterns with our three demonstrated m^{6}A-switch hairpins (Fig. 3f). The RR residues in the RRACH motif and the 3′ U-tract residues show increased structural dynamics in the presence of m^{6}A. Besides, m^{6}A-switches prefer short RRACH–U-tract inter-motif distances, are not involved in the previously reported inter-U-tract motif patterns and are conserved across species (Fig. 3g and Extended Data Fig. 6f–i).

To reveal the function of m^{6}A-switches on RNA biology, we performed polyA$^+$ RNA-seq from *HNRNPC*, *METTL3* and *METTL14* knockdown and control cells (Extended Data Fig. 7a). *METTL3*/*L14* knockdown, which has been shown to decrease HNRNPC binding transcriptome-wide, co-regulated the expression of 5,251 genes with *HNRNPC* knockdown. In comparison, *METTL3*/*L14* knockdown co-regulated only 24 genes with knockdown of another mRNA-binding protein, HNRNPU (Extended Data Fig. 7b), which was not enriched in our m^{6}A-hairpin pull down (Fig. 1b). Approximately 45% of 1,815 high-confidence m^{6}A-switch-containing genes were co-regulated by *HNRNPC* and *METTL3*/*L14* knockdown, indicating that m^{6}A-switch-regulated HNRNPC binding affects the abundance of target mRNAs. Gene ontology (GO) analysis suggests that m^{6}A-switch-regulated gene expression may influence 'cell proliferation' and other biological processes (Extended Data Fig. 7c). The m^{6}A-switch-regulated expression of genes within these GO categories was validated by quantitative polymerase chain reaction (qPCR) (Fig. 4a and Extended Data Fig. 7d–g). We also found that *HNRNPC*, *METTL3* and *METTL14* knockdown decreased the cell proliferation rate to similar extents (Extended Data Fig. 7h).

Besides the mRNA abundance level changes, we also observed splicing pattern changes within high-confidence m^{6}A-switch-containing transcripts by testing the differential exon usage in RNA-seq data (DEXSeq)[30]. *HNRNPC* knockdown co-up/downregulated 131/127 exons with *METTL3* knockdown and 130/115 exons with *METTL14* knockdown. These co-regulated exons occur more frequently in the vicinity of m^{6}A-switches than non-co-regulated exons (Fig. 4b, c), indicating that m^{6}A-switches tend to regulate splicing events at nearby exons. We investigated the splicing pattern at two exons with neighbouring m^{6}A-switches: the PAR-CLIP–MeRIP and *METTL3*/*L14* knockdown data confirmed the HNRNPC-binding signature at the m^{6}A-switch site neighbouring these exons; and *HNRNPC* and *METTL3*/*L14* knockdown co-inhibited exon inclusion in both cases (Fig. 4d–f and Extended Data Fig. 8b–f). Besides, we identified 155 genes with multiple m^{6}A-switches exhibiting more

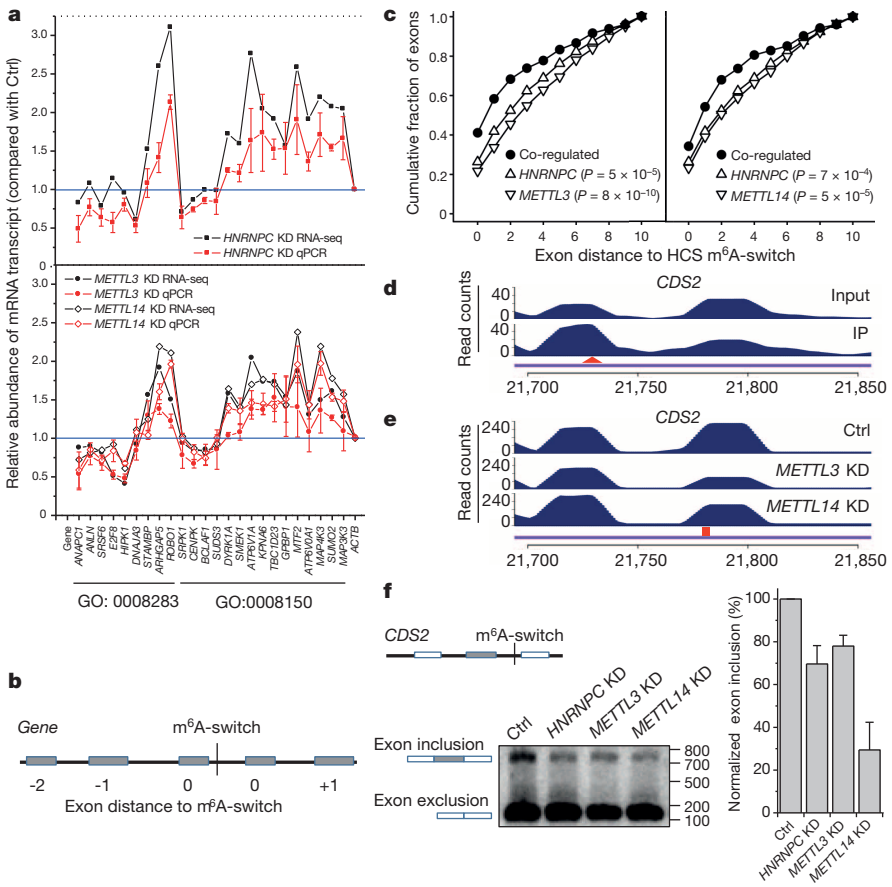

Figure 4 | m^{6}A-switches regulate mRNA abundance and alternative splicing. **a**, *HNRNPC*, *METTL3/L14* knockdown (KD) co-regulated the abundance of m^{6}A-switch-containing transcripts by RNA-seq and qPCR. Ctrl, control. **b**, Illustration of the relative exon distance to m^{6}A-switches. **c**, Co-regulated exons by *HNRNPC* knockdown and *METTL3* knockdown (left) and *METTL14* knockdown (right) were more enriched around m^{6}A-switch sites than non-co-regulated exons, Kolmogorov–Smirnov test. HCS, high confidence m^{6}A-switches. **d**–**f**, Validation of the m^{6}A-switch-regulated splicing at one exon neighbouring the *CDS2* m^{6}A-switch as shown in PAR-CLIP–MeRIP data (**d**), *METTL3/L14* knockdown data (**e**), and PCR with reverse transcription (RT–PCR) results (**f**). The red triangle and square mark the m^{6}A site and U-tract, respectively. Data are mean ± s.d.; $n = 4$, biological replicates.

than two splice variants, and 221 m^{6}A-switch-containing genes with differentially expressed splice variants in *HNRNPC* and *METTL3/L14* knockdown samples. Further analysis suggested that m^{6}A-switches have an effect on intron exclusion (Extended Data Fig. 8g). Consistent with previous reports about splicing regulation by both HNRNPC and m^{6}A[13,19,20,23], our results indicate that m^{6}A functions as an RNA structure remodeller to affect mRNA maturation through interference with post-transcriptional regulator binding activities.

We demonstrated that post-transcriptional m^{6}A modifications could modulate the structure of coding and non-coding RNAs to regulate RNA–HNRNPC interactions, thus influencing gene expression and maturation in the nucleus. It is possible that m^{6}A could also recruit additional accessory factors, such as the YTH domain proteins, which can directly recognize m^{6}A—as previously reported[15]—to destabilize the RNA structure and facilitate HNRNPC binding. Besides HNRNPC, m^{6}A-switches may regulate the function of many other RNA-binding proteins through modulating the RNA-structure-dependent accessibility of their RBMs. Our work indicates widespread m^{6}A-induced mRNA and lncRNA structural remodelling that affects RNA–protein interactions for biological regulation.

Online Content Methods, along with any additional Extended Data display items and Source Data, are available in the online version of the paper; references unique to these sections appear only in the online paper.

Received 24 November; accepted 14 January 2015.

1. Antson, A. A. Single-stranded-RNA binding proteins. *Curr. Opin. Struct. Biol.* **10,** 87–94 (2000).
2. Dreyfuss, G., Kim, V. N. & Kataoka, N. Messenger-RNA-binding proteins and the messages they carry. *Nature Rev. Mol. Cell Biol.* **3,** 195–205 (2002).
3. Ray, D. *et al.* A compendium of RNA-binding motifs for decoding gene regulation. *Nature* **499,** 172–177 (2013).
4. Wan, Y. *et al.* Landscape and variation of RNA secondary structure across the human transcriptome. *Nature* **505,** 706–709 (2014).
5. Ding, Y. *et al. In vivo* genome-wide profiling of RNA secondary structure reveals novel regulatory features. *Nature* **505,** 696–700 (2014).
6. Kertesz, M. *et al.* Genome-wide measurement of RNA secondary structure in yeast. *Nature* **467,** 103–107 (2010).
7. Rouskin, S., Zubradt, M., Washietl, S., Kellis, M. & Weissman, J. S. Genome-wide probing of RNA structure reveals active unfolding of mRNA structures *in vivo*. *Nature* **505,** 701–705 (2014).
8. Bokar, J. A. in *Fine-Tuning of RNA Functions by Modification and Editing* (ed. Grosjean, H.) 141–178 (Springer, 2005).
9. Jia, G. *et al.* N^6-methyladenosine in nuclear RNA is a major substrate of the obesity-associated FTO. *Nature Chem. Biol.* **7,** 885–887 (2011).
10. Zheng, G. *et al.* ALKBH5 is a mammalian RNA demethylase that impacts RNA metabolism and mouse fertility. *Mol. Cell* **49,** 18–29 (2013).
11. Liu, J. *et al.* A METTL3–METTL14 complex mediates mammalian nuclear RNA N^6-adenosine methylation. *Nature Chem. Biol.* **10,** 93–95 (2014).
12. Wang, Y. *et al.* N^6-methyladenosine modification destabilizes developmental regulators in embryonic stem cells. *Nature Cell Biol.* **16,** 191–198 (2014).
13. Dominissini, D. *et al.* Topology of the human and mouse m^{6}A RNA methylomes revealed by m^{6}A-seq. *Nature* **485,** 201–206 (2012).
14. Meyer, K. D. *et al.* Comprehensive analysis of mRNA methylation reveals enrichment in 3′ UTRs and near stop codons. *Cell* **149,** 1635–1646 (2012).
15. Wang, X. *et al.* N^6-methyladenosine-dependent regulation of messenger RNA stability. *Nature* **505,** 117–120 (2014).
16. Fustin, J. M. *et al.* RNA-methylation-dependent RNA processing controls the speed of the circadian clock. *Cell* **155,** 793–806 (2013).
17. Schwartz, S. *et al.* High-resolution mapping reveals a conserved, widespread, dynamic mRNA methylation program in yeast meiosis. *Cell* **155,** 1409–1421 (2013).
18. Batista, P. J. *et al.* m^{6}A RNA modification controls cell fate transition in mammalian embryonic stem cells. *Cell Stem Cell* **15,** 707–719 (2014).
19. Zhao, X. *et al.* FTO-dependent demethylation of N^6-methyladenosine regulates mRNA splicing and is required for adipogenesis. *Cell Res.* **24,** 1403–1419 (2014).
20. König, J. *et al.* iCLIP reveals the function of hnRNP particles in splicing at individual nucleotide resolution. *Nature Struct. Mol. Biol.* **17,** 909–915 (2010).
21. McCloskey, A., Taniguchi, I., Shinmyozu, K. & Ohno, M. hnRNP C tetramer measures RNA length to classify RNA polymerase II transcripts for export. *Science* **335,** 1643–1646 (2012).
22. Rajagopalan, L. E., Westmark, C. J., Jarzembowski, J. A. & Malter, J. S. hnRNP C increases amyloid precursor protein (APP) production by stabilizing APP mRNA. *Nucleic Acids Res.* **26,** 3418–3423 (1998).
23. Zarnack, K. *et al.* Direct competition between hnRNP C and U2AF65 protects the transcriptome from the exonization of Alu elements. *Cell* **152,** 453–466 (2013).
24. Cieniková, Z. *et al.* Structural and mechanistic insights into poly(uridine) tract recognition by the hnRNP C RNA recognition motif. *J. Am. Chem. Soc.* **136,** 14536–14544 (2014).
25. Liu, N. *et al.* Probing N^6-methyladenosine RNA modification status at single nucleotide resolution in mRNA and long noncoding RNA. *RNA* **19,** 1848–1856 (2013).
26. Krecic, A. M. & Swanson, M. S. hnRNP complexes: composition, structure, and function. *Curr. Opin. Cell Biol.* **11,** 363–371 (1999).
27. Görlach, M., Burd, C. G. & Dreyfuss, G. The determinants of RNA-binding specificity of the heterogeneous nuclear ribonucleoprotein C proteins. *J. Biol. Chem.* **269,** 23074–23078 (1994).
28. Kierzek, E. & Kierzek, R. The thermodynamic stability of RNA duplexes and hairpins containing N^6-alkyladenosines and 2-methylthio-N^6-alkyladenosines. *Nucleic Acids Res.* **31,** 4472–4480 (2003).
29. Hafner, M. *et al.* Transcriptome-wide identification of RNA-binding protein and microRNA target sites by PAR-CLIP. *Cell* **141,** 129–141 (2010).
30. Anders, S., Reyes, A. & Huber, W. Detecting differential usage of exons from RNA-seq data. *Genome Res.* **22,** 2008–2017 (2012).

Acknowledgements This work is supported by National Institutes of Health EUREKA GM088599 (C.H. and T.P.), and by K01HG006699 (Q.D.). We thank all members of the Pan and He laboratories for comments and discussions. We also thank Y. C. Leung, G. Perdrizet, Y. Pigli, J. Yue, J. Liu, Y. Yue, K. Chen and M. Yu for technical assistance. C.H. is an Investigator of the Howard Hughes Medical Institute. M.P. was a Natural Sciences and Engineering Research Council of Canada postdoctoral fellow.

Author Contributions N.L., G.Z. and M.P. designed and performed experiments, and analysed data. Q.D. synthesized all RNA oligonucleotides. N.L., M.P. and T.P. conceived the project. N.L. and T.P. wrote the paper with input from C.H. and M.P.

Author Information RNA-seq data have been deposited in the Gene Expression Omnibus under accession number GSE56010. Reprints and permissions information is available at www.nature.com/reprints. The authors declare no competing financial interests. Readers are welcome to comment on the online version of the paper. Correspondence and requests for materials should be addressed to M.P. (marc.parisien@mcgill.ca) or T.P. (taopan@uchicago.edu).

METHODS

Mammalian cell culture, siRNA knockdown and western blot. Human cervical cancer cell line HeLa (CCL-2) and embryonic kidney cell line HEK293T (CRL-11268) were obtained from the American Type Culture Collection (ATCC) and were cultured under standard conditions. Control short interfering RNA (siRNA) (1027281, Qiagen), *METTL3* siRNA (SI04317096, Qiagen), *METTL14* siRNA (SI04317096, Qiagen) or *HNRNPC* siRNA (10620318, Invitrogen) were transfected into HEK293T cells at a concentration of 40 nM using lipofectamine RNAiMAX (Invitrogen) according to the manufacturer's instructions. Cells were collected 48 h after the transfection, shock-frozen in liquid nitrogen, and stored at −80 °C for further studies. Western blot analysis using METTL3- (HPA038002, Sigma), METTL14- (HPA038002, Sigma), HNRNPC- (sc-32308, Santa Cruz) and GAPDH- (A00192-40, Genescript) specific antibodies was performed under standard procedures. Blotting membranes were stained by ECL-prime (RPN2232, GE Healthcare) and visualized by a digital imaging system (G: BOX, SYNGENE). All synthetic oligonucleotides were synthesized by Q.D.

Gel shift, RNA pull-down and filter-binding assays. HeLa nuclear extracts were isolated using the NE-PER Nuclear and Cytoplasmic Extraction Reagents (78833, Thermo Scientific) according to the manufacturer's instructions. The purified radioactively labelled RNA oligonucleotides were refolded by heating at 90 °C for 1 min, then at 30 °C for 5 min. Three microlitres HeLa nuclear extract and 6 μl refolded RNA were incubated at room temperature for 30 min and then at 4 °C for 2 h. Each sample was mixed with 1 μl 50% glycerol, separated on an 8% native 1× TBE gel, and visualized by phosphorimaging using the Personal Molecular Imager (Bio-Rad).

The *in vitro* pull-down assay was performed as described[13]. The eluted protein samples were separated on 4–12% polyacrylamide Bis-Tris gels (NP0321BOX, Invitrogen) and stained with SYPRO-Ruby (S12000, Invitrogen) according to the manufacturer's instructions. Protein in gel slices or the entire pulled-down protein samples were digested with trypsin and identified using Liquid chromatography-tandem mass spectrometry by the Donald Danforth Plant Science Center (Washington University). The RNA oligonucleotides used in Fig. 1f were: 2,577–U, 5′-A ACUUAAUGUUUUUGCAUUGGUCUUUGAGUUA-Biotin; 2,577–CC-A, 5′- A ACUUAAUGUCCUUGCAUUGGACUUUGAGUUA-Biotin; 2,577–CC-m^{6}A, 5′- AACUUAAUGUCCUUGCAUUGGm^{6}ACUUUGAGUUA-Biotin.

The full-length HNRNPC1 protein was purified and the *in vitro* ultraviolet cross-linking assay was performed as previously described[23]. Filter-binding assays were performed as previously described[24].

CLIP-2dTLC. HEK293T cells at 70–80% confluency were ultraviolet irradiated with 400 mJ cm^{-2} at 254 nm, and harvested by centrifuging at 4,000 r.p.m. for 3 min at 4 °C (with centrifugation rotor 75003524, Fisher Scientific). The pellet of cross-linked cells were resuspended in 1 ml lysis buffer (1× PBS, 0.1% SDS, 1% Nonidet P-40, 0.5% sodium deoxycholate, protease inhibitor cocktail and RNase inhibitor) and incubated on ice for 4 h. Cell lysate was isolated by centrifuging at 3,000 r.p.m. for 5 min and pre-blocked with 50 μl protein A beads in 300 μl lysis buffer. Another 50 μl protein A beads (Invitrogen) were incubated with 8 μg corresponding antibodies for 4 h at room temperature, and then mixed with the pre-blocked cell lysate at 4 °C overnight. The beads were washed three times with 1 ml wash buffer (20 mM Tris-HCl pH 7.4, 10 mM $MgCl_2$, 0.2% Tween-20), three times with 1 ml high-salt buffer (5× PBS, 0.1% SDS, 1% Nonidet P-40, 0.5% sodium deoxycholate), and three times with 1 ml wash buffer. The beads were resuspended in 1 ml wash buffer, and divided into 2× 500 μl in two separate tubes. One tube was incubated with 200 μl RNase T1/A mixture at room temperature for 1 h. The other tube was incubated with 200 μl nuclease-free water at room temperature for 1 h. The beads were washed three times with 1 ml high-salt buffer, and three times with 1 ml wash buffer. Cross-linked RNA was eluted from beads by incubating with 200 μl RNA elution buffer (100 mM Tris-HCl pH 7.4, 10 mM EDTA, 1% SDS) containing 2 mg ml^{-1} proteinase K at 50 °C for 30 min followed by phenol/chloroform extraction. The RNA pellet was dissolved in 7 μl nuclease-free water containing 1 μl RNase T1 (200 U), heated at 65 °C for 2 min, and incubated at 37 °C for 30 min. The T1-digested RNA fragments were labelled upon adding 2 μl T4 PNK mix (4.5 U μl^{-1} T4 PNK, 600 Ci mmol^{-1} [γ-^{32}P] ATP, 5× PNK buffer) and incubation at 37 °C for 30 min. Unreacted [γ-^{32}P] ATP was removed using Illustra MicroSpin G-25 columns. The eluted RNA was digested with 1 μl (1 U μl^{-1}) nuclease P1 at 37 °C for 1 h. Samples were spotted on cellulose TLC plate and 2dTLC was run as described[25] using isobutyric acid: 0.5 M NH_4OH (5:3, v/v) as the first dimension and isopropanol:HCl:water (70:15:15, v/v/v) as the second dimension.

RNA structural probing and RNA terminal truncation. The synthetic RNA oligonucleotides were 5′-end-labelled with γ-^{32}P-ATP by T4 PNK (70031, Affymetrix), gel purified, and re-folded. Structural probing assay with RNase T1, nuclease S1 and RNase V1 was performed as previously described[25]. Note that 3′-end-labelled *HNRNPH1* oligonucleotides were used for the RNA structural probing assay shown in Fig. 2g.

CMCT RNA structural probing assay was performed as reported[31]. RNA refolding: 3 pmol RNA was annealed in 50 mM potassium borate (pH 8) by heating at 90 °C for 1.5 min then incubation at room temperature for 3 min.

RNA terminal truncation assay was carried out as previously reported[32]. RNA samples were first alkaline-hydrolysed as in the RNA structural probing assay, and then incubated with HNRNPC1 protein in the same conditions as in the filter binding assay. The RNA–protein complexes were then loaded onto filter papers and washed twice with chilled binding buffer. Air-dry filters and RNA samples were then extracted from the filters and loaded onto denaturing gel as in the RNA structural probing assay.

PAR-CLIP and PAR-CLIP–MeRIP. PAR-CLIP procedures were performed as previously reported[29] with the following modification. HEK293T cells in 15-cm plates treated following normal PAR-CLIP procedures were lysed and digested with a combination of RNase I (Ambion, AM2295, 15 μl 1/50 diluted with H_2O) and Turbo DNases (2 μl) for 3 min at 37 °C, shaking at 1,100 r.p.m. The lysate was then immediately cleared by spinning at 14,000 r.p.m., 4 °C for 30 min, and placed on ice for further use. HNRNPC-binding sites were identified by PARalyzer v.1.1 (ref. 33) with default settings.

PAR-CLIP–MeRIP experiment applied m^{6}A-antibody immunoprecipitation[13,14,34] to the HNRNPC PAR-CLIP RNA samples. The HNRNPC PAR-CLIP RNA sample was incubated with m^{6}A-specific antibody (202003, SYSY), RNase inhibitor (80 units, Sigma-Aldrich), human placental RNase inhibitor (NEB) in 200 μl 1× IP buffer (50 mM Tris-HCl pH 7.4, 750 mM NaCl and 0.5% (v/v) Igepal CA-630) at 4 °C for 2 h under gentle shaking conditions. For each PAR-CLIP–MeRIP experiment, 20 μl protein A beads (Invitrogen) were washed twice with 1 ml 1× IP buffer, blocked with 2 h incubation with 100 μl 1× IP buffer supplemented with bovine serum albumin (BSA) (0.5 mg ml^{-1}), RNasin and human placental RNase inhibitor, and then washed twice with 100 μl 1× IP buffer. The pre-blocked protein A beads were then combined with the prepared immuno-reaction mixture and incubated at 4 °C for 2 h, followed by three washes with 100 μl 1× IP buffer. After that, the RNA was eluted by 1 h incubation with 20 μl elution buffer (1× IP buffer and 6.7 mM m^{6}A, Sigma-Aldrich) under gentle shaking conditions, and purified by ethanol precipitation. The purified RNA sample (IP) as well as the input PAR-CLIP RNA sample (input control) were used for library construction by Truseq small RNA sample preparation kit (Illumina).

Libraries were prepared using TruSeq Small RNA Sample Preparation Kit (RS-200-0012, Illumina) according to the manufacturer's instructions, and then sequenced by Illumina Hiseq2000 with single-end 50-bp read length. The control and IP samples from PAR-CLIP–MeRIP experiments (same case for the control and knockdown samples from *METTL* knockdown experiments) were sequenced together in one flowcell on two lanes, and the reads from two lanes of each sample were combined for remaining analysis. The raw sequencing data were trimmed using the Trimmomatic computer program v.0.30 (ref. 35) to remove adaptor sequences, and mapped to the human genome version hg19 by Bowtie 1.0.0 (ref. 36) without any gaps and allowed for at most two mismatches.

Detection of PAR-CLIP–MeRIP peaks and differential PAR-CLIP peaks. The raw read counts of the biological replicates confirmed the reproducibility between replicates (Extended Data Fig. 9), and replicates were combined for subsequent analysis. For each genomic site, we calculated the average read counts within an 11-nucleotide window centred at that site, as the normalized read counts for that site. This normalization smoothed the raw mapping curves, and facilitated identification of peaks within each mapping cluster. To correct for changes in sequencing depth or expression levels between samples, we then normalized the read counts at each genomic site to the total number of read counts on the respective gene. The above defined double-normalization procedures enabled precise identification of changes in the mapping reads at specific genomic locations by directly comparing the normalized read counts between samples. No read counts in the intergenic region were compared between samples, because the transcription boundaries are not defined at this region and the intergenic read counts cannot be normalized to correct changes for transcript expression.

Detection of PAR-CLIP–MeRIP peaks involves comparing the read counts of the IP sample with that of the control (Ctrl) sample as follows: (1) we identified all peaks within HNRNPC-binding sites in the IP sample; (2) we performed transcriptome-wide scanning to compare read counts of each identified peak in (1) with read counts at the same genomic locations in the Ctrl sample to calculate the fold change score, score = $\log_2$ (H_{IP}/H_{Ctrl}). The score threshold was set to be 1, corresponding to a twofold increase compared with control.

The detection of decreased HNRNPC-binding sites involved comparing HNRNPC occupancies in the *METTL* knockdown (KD) sample with that in the control as follows: (1) we identified all peaks within HNRNPC-binding sites in the *METTL* knockdown sample; (2) we performed transcriptome-wide scanning to compare read counts of each identified peak in (1) with read counts at the same genomic locations in control to calculate the fold change score, score = $\log_2$ (H_{KD}/H_{Ctrl}).

The score threshold was set to be −1, corresponding to a twofold decrease compared with control.

Identification of enriched motifs and HNRNPC m^{6}A-switches. To identify enriched motifs, we first sorted the 12,998 HNRNPC PAR-CLIP–MeRIP peaks (with IP/input enrichment ≥ 2) by the T-to-C mutation frequency. We then chose the top 4,500 peaks with the highest T-to-C mutation frequency for motif analysis using FIRE[37] with default RNA analysis parameters. The top two enriched motifs are the GRACH and the U-tract motif. We also used the top 1,024 and 2,048 peaks for motif analysis, yielding the same motif results as the top 4,500 peaks.

To identify transcriptome-wide HNRNPC m^{6}A-switches, we first searched for all coupling events within 50 nucleotides between U_5 and RRACH motifs, with the U_5 motif located within HNRNPC-binding sites. For PAR-CLIP–MeRIP samples, the fold-change score E at the RRACH motif was calculated for each coupling event. Also, the P value for each coupling event was calculated as described[38]. Then, we generated the π value, $\pi = E\cdot(-\log_{10} P)$, as one comprehensive parameter to pick meaningful genomic loci[39]. HNRNPC m^{6}A-switches identified from PAR-CLIP–MeRIP experiments should fulfill the following requirements: (1) read counts at both the control and IP sample ≥ 5; (2) π value ≥ 0.627, corresponding to FDR ≤ 5%.

For *METTL* knockdown samples, the fold-change score at the U-tract motifs was calculated for each coupling event. HNRNPC m^{6}A-switches identified from *METTL3/L14* knockdown samples should fulfil the following requirements: (1) read counts at both the control and knockdown sample ≥ 5; (2) π value ≤ 0.627, corresponding to FDR ≤ 5%.

Distribution of HNRNPC m^{6}A-switches. Pie charts illustrating the distribution within each segment were made using the following hierarchy: intron > ncRNA > 3′ UTR > 5′ UTR > CDS > intergenic. To plot the distribution of HNRNPC m^{6}A-switches in their respective localized segments (such as intron, exon, 3′ UTR, CDS, 5′ UTR), we first identified the distance between each m^{6}A-switch and the 5′ end of the respective segment. This distance was then divided by the length of that segment to determine a percentile where this m^{6}A-switch fell, and then this specific percentile bin was incremented. Following this approach, we obtained the distribution pattern of all m^{6}A-switches within each segment.

RNA-seq. RNA-seq experiments were performed on two replicate RNA samples from *HNRNPC*, *METTL3*, *METTL14* knockdown as well as control HEK293T cells (48 h after transfection). Total RNA samples were extracted according to the RNeasy Plus Kit (catalogue no. 74104, Qiagen). Libraries were prepared according to the TruSeq Stranded mRNA LT Sample Prep Kit (catalogue no. RS-122-9005DOC). Knockdown and control samples were sequenced together in one flowcell on four lanes, respectively. All samples were sequenced by illumina Hiseq 2000 with pair end 100-bp read length. The reads from the four lanes of each sample were combined for all analyses. The RNA-seq data were mapped using the splice-aware alignment algorithm TopHat v.1.1.4 (ref. 40) based on the following parameters: tophat -num-threads 8 -mate-inner-dist 200 -solexa-quals -min-isoform-fraction 0 -coverage-search-segment-mismatches 1. Gene expression level changes were analysed using cuffdiff[41]. Differential splicing was determined using DEXSeq[30] based on Cufflinks-predicted, non-overlapping exons. To compare with a different mRNA-binding protein, the RNA-seq data from *HNRNPU* knockdown HEK293T cells (GEO34995 data set[42]) were analysed.

GO, evolutionary conservation, graphic and statistical analyses. GO enrichment analysis was applied on the co-regulated high-confidence m^{6}A-switch-containing genes, against all high-confidence m^{6}A-switch-containing genes as background, using GOrilla[43].

Phylogenetic conservation analysis was performed by comparing PhyloP scores at the U-tract motif and RRACH motif for HNRNPC m^{6}A-switches to those of randomly selected sequences. The PhyloP scores were accessed from the precompiled PhyloP scores[44] (ftp://hgdownload.soe.ucsc.edu/goldenPath/hg19/phyloP46way/) under both primate and vertebrate categories. P values were evaluated using the Mann–Whitney–Wilcoxon test, $***P < 10^{-16}$. For the U-tract motifs, we collected all U-tracts (5× Us) across all chromosomes and randomly selected 10,000 sites among the 38,561,577 sites of our census. The random selection was done separately for primates and for vertebrates. For the RRACH motif, we also collected all RRACH sites across all chromosomes and randomly selected 10,000 sites among the 78,815,225 sites of our census. Here, too, the random selection was done separately for primates and vertebrates.

Sequence logos were generated using the WebLogo package. The R statistical package was used for all statistical analyses (unless stated otherwise).

Cell proliferation analysis. HEK293T cells were transfected with si-control, si-*HNRNPC*, si-*METTL3* and si-*METTL14* RNAs. After transfection, the numbers of cells were counted at 0, 24, 48 and 72 h, as described previously[45]. Three independent experiments were performed and growth curves were plotted to test the effects on cell proliferation.

RT–PCR quantitation. Total RNA samples were extracted from HEK293T cells and reverse transcribed using SuperScript III First-Strand Synthesis System (Life Technologies, catalogue no. 18080-051). In order to validate the splicing changes identified from our RNA-seq data, we performed RT–PCR measurements using Thermo Scientific Taq DNA Polymerase under the following conditions: 95 °C for 3 min, 30 cycles of 95 °C for 30 s, 55 °C for 30 s, 72 °C for 1 min, and then finally 72 °C for 10 min. For the target alternate exon, we designed and used primers annealing to both neighbouring constitutive exons. The PCR products were separated on 1.2% agarose gel and ethidium bromide stained. In order to validate the gene expression level changes identified from our RNA-seq data, we performed qRT–PCR measurements using Power SYBR Green PCR Master Mix (Life Technology, catalogue no. 4367659) under the following conditions: 50 °C for 3 min followed by 95 °C for 10 min, 40 cycles of 95 °C for 15 s, 60 °C for 1 min, and then 40 °C for 1 min and 95 °C for 15 s and finally 60 °C for 30 s.

The primer sequences are as follows (listed as gene name: forward primer; reverse primer). *ANAPC1*: TGCCAAAAGAAATAGCAGTTCAG; TGCCAAAAGAAATAGCAGTTCAG; *ANLN*: GCCAGGCGAGAGAATCTTCA; GGCTGCTGGTTACTTGCTTC; *SRSF6*: ACAAGGAACGAACAAATGAGGG; GCTTCCAGAGTAAGATCGCCTAT; *E2F8*: ACCCAAGCTCAGCCATTGTA; GAGTCATAGTTGGTGGCCCT; *HIPK1*: CCAGTCAGCTTTGTACCCATC; TTGAAACGCAGGTGGACATA; *DNAJA3*: CCCTTTCATTTGTACTGCCTCC; TGATCTCTTTCTGGCTGGCA; *STAMBP*: GTTCTCATCCCCAAGCAAAG; ATCCAGCCCAGTGTGATGA; *ARHGAP5*: GCGGATTCCATTTGACCTCC; GCTGCCCTGGTGAAATGAAT; *ROBO1*: TTTGGGCTTCTGCGTAGTTT; GGAGGGTACTGGAGACAGCA; *SRPK1*: CCCTGAGAAGAGAGCCACTG; ACCCTGAAAAGGGAAGAGGA; *CENPK*: AAGGCTAAAAATTCACAAAGCA; TCCATATCTTTCCACATTTCTTCA; *BCLAF1*: TCCTGAAAGGTCTGGGTCTG; TCCTGAAAGGTCTGGGTCTG; *SUDS3*: TGCCTGGGGTTCTGTATTTC; CAGTTCAAGCGAGGGAAGTC; *DYRK1A*: CTTCAGCATGCAAACCTTCA; GGCAGAAACCTGTTGGTCAC; *SMEK1*: TTGAAGGACTGCACCACTTG; CCTGTGTTTTCGTGGTTGTG; *ATP6V1A*: AAGCATTTCCCCTCTGTCAA; CTGCCAGGTCTTCTTCTTCC; *KPNA6*: CCCTGTGTTGATCGAAATCC; GATCTGCTCAGGGGTTCCTC; *TBC1D23*: GGTGAATCTCCTAATGGCTCA; CGATCCACAGGAGTTGATGT; *GPBP1*: CGTCATTGAATTTTGAGAAGCA; TTAGGACGCCCAATAGCAGA; *MTF2*: GTCTGCATTTGGTTCCTGGT; CTGCAGGAAAGGCAACCTTA; *ATP6V0A1*: TCCGTGTCTGGTTCATCAAA; TCTGAGTGCAAACTGGATGG; *MAP4K3*: TCTTCATACCACAGGAAATGC; AACAGGTTTGTGTGGGGGTA; *SUMO2*: TTCTTTCATTTCCCCCTTCC; TATTTTTCCCCATCCCGTCT; *MAP3K3*: CAGTTCCTCTCCCCACTCTG; GACAGAGAGGTGCCTGCTTC; *CDS2*: CGATTTTCCCAGGATGACAG; GAAAGGGCCCTATTGAGGAC; *YTHD1F2*: ACTTGAGTCCACAGGCAAGG; AAGCAGCTTCACCCAAAGAA.

31. Ehresmann, C. *et al.* Probing the structure of RNAs in solution. *Nucleic Acids Res.* **15,** 9109–9128 (1987).
32. Peterson, E. T., Pan, T., Coleman, J. & Uhlenbeck, O. C. *In vitro* selection of small RNAs that bind to *Escherichia coli* phenylalanyl-tRNA synthetase. *J. Mol. Biol.* **242,** 186–192 (1994).
33. Corcoran, D. L. *et al.* PARalyzer: definition of RNA binding sites from PAR-CLIP short-read sequence data. *Genome Biol.* **12,** R79 (2011).
34. Dominissini, D., Moshitch-Moshkovitz, S., Salmon-Divon, M., Amariglio, N. & Rechavi, G. Transcriptome-wide mapping of N^6-methyladenosine by m^{6}A-seq based on immunocapturing and massively parallel sequencing. *Nature Protocols* **8,** 176–189 (2013).
35. Lohse, M. *et al.* RobiNA: a user-friendly, integrated software solution for RNA-Seq-based transcriptomics. *Nucleic Acids Res.* **40,** W622–W627 (2012).
36. Langmead, B., Trapnell, C., Pop, M. & Salzberg, S. L. Ultrafast and memory-efficient alignment of short DNA sequences to the human genome. *Genome Biol.* **10,** R25 (2009).
37. Elemento, O., Slonim, N. & Tavazoie, S. A universal framework for regulatory element discovery across all genomes and data types. *Mol. Cell* **28,** 337–350 (2007).
38. Ouyang, Z., Snyder, M. P. & Chang, H. Y. SeqFold: genome-scale reconstruction of RNA secondary structure integrating high-throughput sequencing data. *Genome Res.* **23,** 377–387 (2013).
39. Xiao, Y. *et al.* A novel significance score for gene selection and ranking. *Bioinformatics* **30,** 801–807 (2014).
40. Trapnell, C., Pachter, L. & Salzberg, S. L. TopHat: discovering splice junctions with RNA-Seq. *Bioinformatics* **25,** 1105–1111 (2009).
41. Trapnell, C. *et al.* Differential gene and transcript expression analysis of RNA-seq experiments with TopHat and Cufflinks. *Nature Protocols* **7,** 562–578 (2012).
42. Huelga, S. C. *et al.* Integrative genome-wide analysis reveals cooperative regulation of alternative splicing by hnRNP proteins. *Cell Rep.* **1,** 167–178 (2012).
43. Eden, E., Navon, R., Steinfeld, I., Lipson, D. & Yakhini, Z. GOrilla: a tool for discovery and visualization of enriched GO terms in ranked gene lists. *BMC Bioinformatics* **10,** 48 (2009).
44. Pollard, K. S., Hubisz, M. J., Rosenbloom, K. R. & Siepel, A. Detection of nonneutral substitution rates on mammalian phylogenies. *Genome Res.* **20,** 110–121 (2010).
45. Yang, F., Yi, F., Han, X., Du, Q. & Liang, Z. MALAT-1 interacts with hnRNP C in cell cycle regulation. *FEBS Lett.* **587,** 3175–3181 (2013).

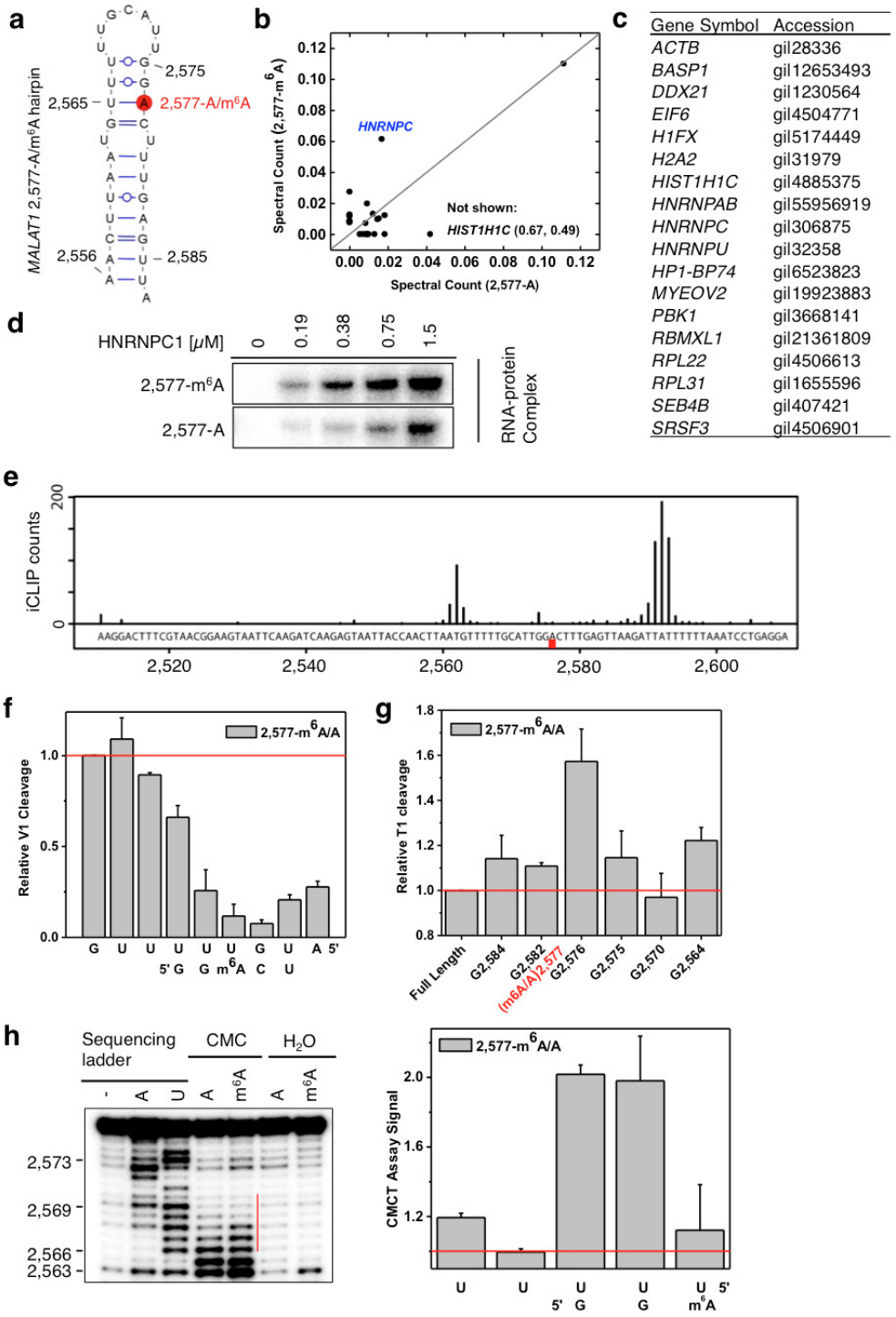

Extended Data Figure 1 | m^{6}A increases the accessibility of the U-tract to enhance HNRNPC binding. **a**, Secondary structure of the *MALAT1* hairpin with m^{6}A methylation at the 2,577 site shown in red[25]. Nucleotide position numbers correspond to their locations along the human *MALAT1* transcript (NCBI accession NR_002819). **b**, RNA pull down showing that HNRNPC preferably binds methylated RNA. **c**, The list of proteins with identified peptides by mass spectrometry in **b**. **d**, Recombinant HNRNPC1 binds more strongly with that *MALAT1* 2,577–m^{6}A hairpin compared with the unmethylated hairpin, as determined by an *in vitro* ultraviolet crosslinking assay[23]. **e**, HNRNPC shows binding around the 2,577–A site along *MALAT1* *in vivo*, as determined by previously published HNRNPC iCLIP data[20]. The underlying genomic sequence is shown at the bottom with a red square marking the 2,577–m^{6}A site. The slight shift of the iCLIP signal to upstream of the U-tract-binding site is probably due to the steric hindrance of the peptide fragment remaining on RNA, which can cause reverse transcription to terminate more than one nucleotide upstream of the crosslink site[20]. **f**, Quantification of the RNase V1 cleavage signal for the U-tract region from the RNA structural mapping assay in Fig. 1e. To correct for sample loading difference, each band signal was normalized to the band signal of the immediate 3′ residue to the U-tract. Data are mean ± s.d.; $n = 3$, technical replicates. **g**, Quantitative analysis of the RNase T1 cleavage signal from the RNA structural mapping assay in Fig. 1e. An increased RNase T1 cleavage signal (single-strand specific and cleavage after guanosines) was observed due to the surrounding m^{6}A residue. To correct for sample loading difference, the ratio for each band signal among all bands in each lane was calculated. Relative T1 cleavage = $(m^6A_{native}/m^6A_{denature})/(A_{native}/A_{denature})$. $n = 2$, technical replicates. **h**, Quantitative CMCT mapping showing increased signals for the U-tract bases around the U base-pairing with m^{6}A. Quantitation of band signals within the U-tract region is shown on the right. Data are mean ± s.d.; $n = 4$, technical replicates.

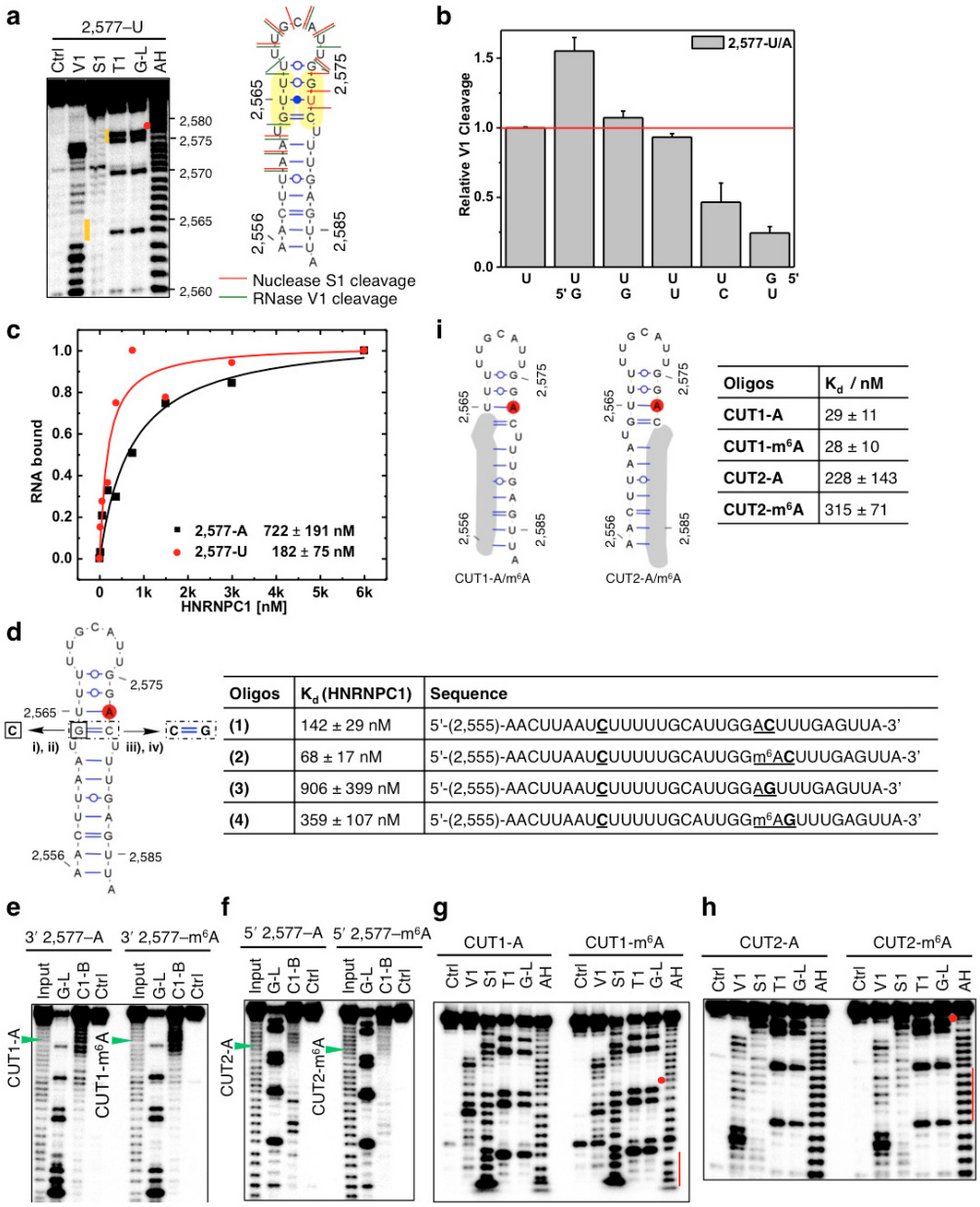

Extended Data Figure 2 | Increased accessibility of U-tracts enhances HNRNPC binding. **a**, Structure probing of the 2,577–A-to-U mutated MALAT1 hairpin (2,577–U). The annotation is the same as in Fig. 1d. **b**, Quantification of the RNase V1 cleavage signal for the U-tract region from RNA structural mapping assays as in **a**. To correct for sample loading difference, each band signal was normalized to the band signal of the 3′-most U of the U-tract. $n = 2$, technical replicates. **c**, Filter-binding curves displaying the binding affinities between recombinant HNRNPC1 and 2,577–U/A oligonucleotides. Data are mean ± s.d.; $n = 3$, technical replicates. **d**, Filter-binding results showing the binding affinities between recombinant HNRNPC1 and four mutated *MALAT1* oligonucleotides. (1) Mutate G–C to C–C, 2,577–A: predicted to weaken the hairpin stem and increase HNRNPC binding. Results: binding improved from 722 nM K_d to 142 nM (fivefold). (2) Mutate G–C to C–C, 2,577–m^{6}A: in this context of weaker stem, m^{6}A is predicted to confer a smaller effect compared to wild-type hairpin. Result: improved binding only twofold instead of eightfold. (3) Restore C–C to C–G, 2,577–A: predicted to restore the hairpin stem and decrease HNRNPC binding compared to C–C mutant. Result: binding decreased by 6.4-fold. (4) Restore C–C to C–G, 2,577–m^{6}A: in this context of restored stem, m^{6}A is again predicted to confer increased binding compared to 2,577–A hairpin. Result: improved binding by 2.5-fold. Data are mean ± s.d.; $n = 3$ each, technical replicates. **e**, RNA alkaline hydrolysis terminal truncation assay showing recombinant HNRNPC1 binding to terminal truncated *MALAT1* hairpin oligonucleotides (2,577 site m^{6}A methylated or unmethylated). In this assay, 3′-radiolabelled *MALAT1* 2,577 hairpin oligonucleotides were terminal truncated by alkaline hydrolysis into RNA fragments that were then incubated with HNRNPC1 protein followed by filter binding wash steps. The remaining RNA on the filter paper was isolated and analysed by denaturing gel electrophoresis, as indicated in the lane 'C1-bound or C1-B'. 'Input' refers to alkaline-hydrolysis-truncated RNA oligonucleotides used for incubation with hnRNP C1; 'G-L or G-ladder' was generated from RNase T1 digestion; 'Ctrl' refers to the intact *MALAT1* hairpin without alkaline hydrolysis truncation. One pair of methylated/unmethylated truncated oligonucleotides (CUT1, marked by green arrows) was selected for subsequent biochemical analysis, due to their strong interaction with HNRNPC1. **f**, RNA terminal truncation assay as in **e** except 5′ ^{32}P-labelled oligonucleotides were used. One pair of methylated/unmethylated truncated oligonucleotides (CUT2, marked by green arrows) was selected for subsequent biochemical analysis. **g**, Structure probing of the CUT1 oligonucleotides using RNase V1 and nuclease S1 digestion. Annotation is the same as in Fig. 1e. The red dot marks the m^{6}A site and the red line marks the U-tract region. **h**, Structure probing of the CUT2 oligonucleotides using RNase V1 and nuclease S1 digestion. Annotation is the same as in **g**. **i**, Truncated oligonucleotides with exposed U-tracts increased HNRNPC binding regardless of m^{6}A. Data are mean ± s.d.; $n = 3$, technical replicates.

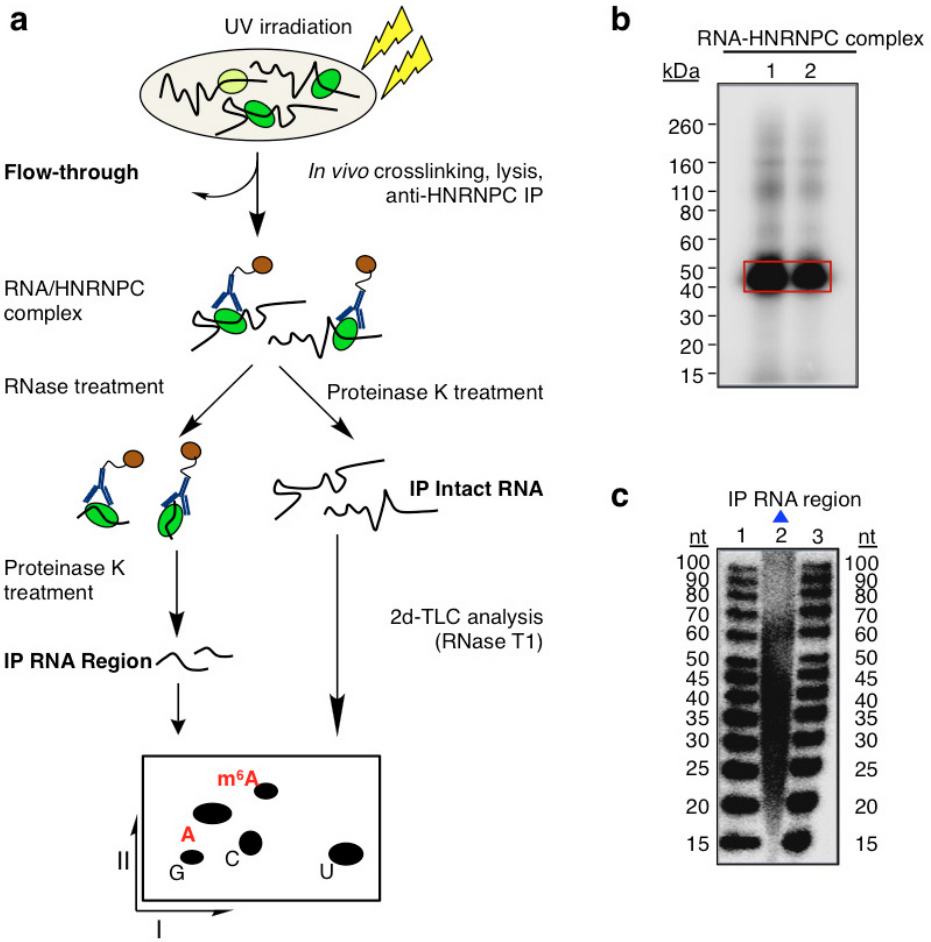

Extended Data Figure 3 | m^{6}A is enriched in the vicinity of HNRNPC-binding sites. **a**, Schematic diagram of the CLIP-2dTLC protocol. IP, immunoprecipitation; nt, nucleotide; UV, ultraviolet. The RNase T1 used in our 2dTLC assay cleaves single-stranded RNA after guanosines, so the m^{6}A/A ratio determined here represents the m^{6}A fraction of all adenosines following guanosines. **b**, Analysis of crosslinked RNA–HNRNPC complexes (CLIP RNP) using denaturing gel electrophoresis (lanes 1 and 2). Positions of the protein size standards are shown on the left. HNRNPC IP RNA region (RNA samples within RNA–HNRNPC crosslinked complexes) were extracted from the gel slices marked by the red rectangle. **c**, Denaturing gel analysing the size distribution for the HNRNPC PAR-CLIP RNA samples (lane 2). The RNA size standards were loaded in lanes 1 and 3.

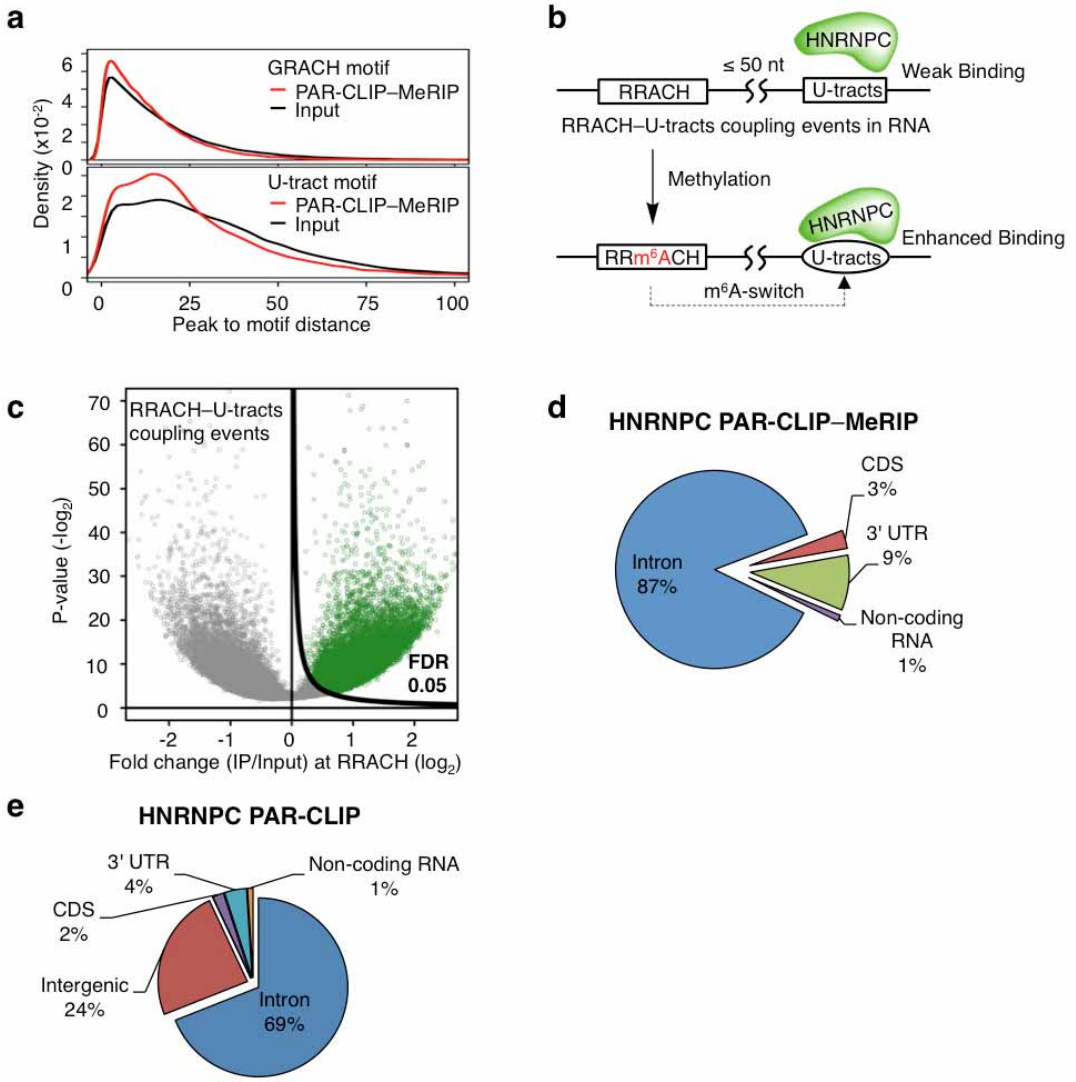

Extended Data Figure 4 | PAR-CLIP–MeRIP identifies transcriptome-wide m^{6}A-switches in the vicinity of HNRNPC-binding sites. **a**, Density plots illustrating the distribution of distance between the PAR-CLIP–MeRIP/input peaks and the nearest GRACH motif (top) or the nearest U-tracts (bottom). **b**, Definition and identification of HNRNPC m^{6}A-switches based on the PAR-CLIP–MeRIP analysis. Approximately 89% of PAR-CLIP–MeRIP peaks harbouring both the U-tract and RRACH motifs have an RRACH–U-tract inter-motif distance within 50 nucleotides, significantly higher than the 64% of such coupling within the genomes. HNRNPC m^{6}A-switches are identified as m^{6}A-methylated RRACH–U-tract coupling events. **c**, Volcano plot depicting all coupling events (open circles) as defined in **b**, according to their *P* values[36] (*P*; *y* axis) and fold-change values at RRACH sites (*E*; *x* axis). To identify HNRNPC m^{6}A-switches, we generated the π value, $\pi = E\cdot(-\log_{10}P)$, as one comprehensive parameter to pick meaningful genomic loci[37]. HNRNPC m^{6}A-switches identified from PAR-CLIP–MeRIP experiments should fulfil the following requirements: (1) read counts at both the control and IP sample ≥ 5; (2) π value ≥ 0.627, corresponding to FDR $\leq 5\%$. **d**, Pie chart depicting the region distribution of HNRNPC m^{6}A-switches identified by PAR-CLIP–MeRIP. **e**, Pie chart depicting HNRNPC PAR-CLIP peaks. These are enriched in introns, consistent with previous reports that HNRNPC binds mainly nascent transcripts[19,23,25].

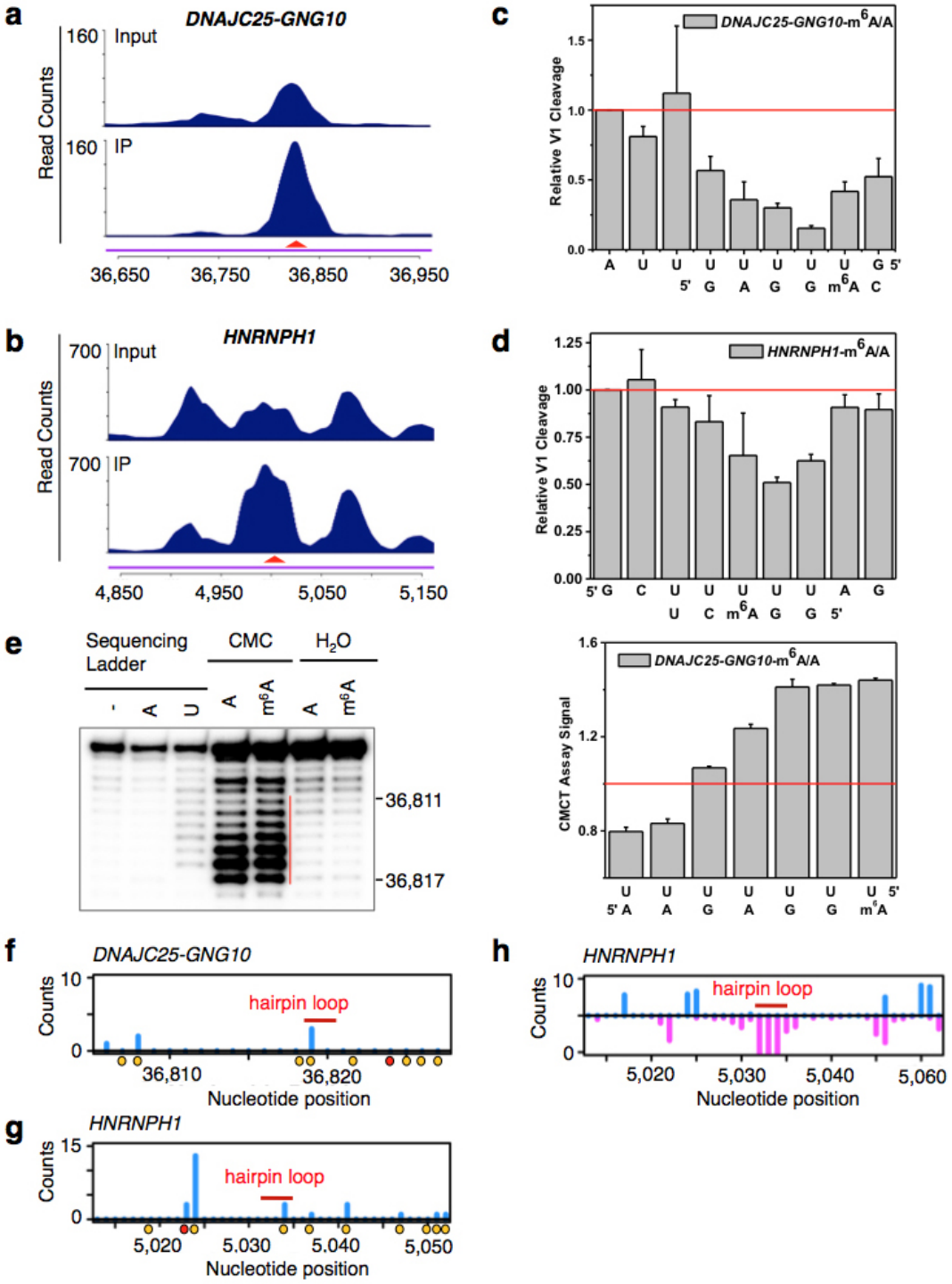

Extended Data Figure 5 | Validation of two identified m^{6}A-switches. **a**, **b**, PAR-CLIP–MeRIP data detected positive IP/input enrichment at the RRACH sites (red arrowheads) on the *DNAJC25-GNG10* gene (**a**) and *HNRNPH1* gene (**b**) in HEK293T cells. **c**, **d**, Quantification of RNase V1 cleavage signals around the U-tract region of m^{6}A-switches on the *DNAJC25-GNG10* (**c**) and *HNRNPH1* (**d**) transcript, related to Fig. 2g, h. Data are mean ± s.d.; $n = 3$, technical replicates each. **e**, Quantitative CMCT mapping of *DNAJC25-GNG10* m^{6}A-switch shows increased band signals around the uridine base that pairs with m^{6}A. The red vertical line marks the U-tract region. Quantitation of band signal for the U-tract region is shown on the right. Data are mean ± s.d.; $n = 3$, technical replicates. The *HNRNPH1* m^{6}A-switch hairpin is not suitable for CMCT probing, because its reverse transcription binding primer region is too short. **f**, **g**, *In vivo* DMS mapping of the *DNAJC25-GNG10* hairpin (**f**) and *HNRNPH1* (**g**); data are from ref. 7. A and C residues are marked with orange dots and the m^{6}A residue is marked with a red dot. The hairpin loops are indicated by red bars. **h**, Transcriptome-wide S1/V1 mapping around the *HNRNPH1* m^{6}A-switch site. Blue bars represent V1 signal; magenta bars represent S1 signal. The hairpin loop is indicated by a red bar; data are from ref. 4. Not enough reads could be collected to make a plot for the *DNAJC25-GNG10* m^{6}A-switch region.

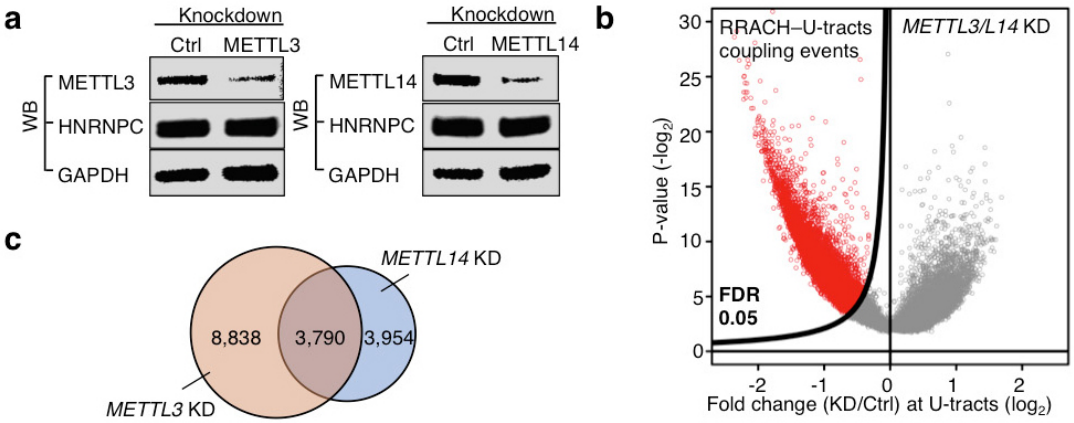

d

HCS fraction	Exon	Intron
Coding RNA	16.67%	83.32%
Non-coding RNA	24.39%	75.61%

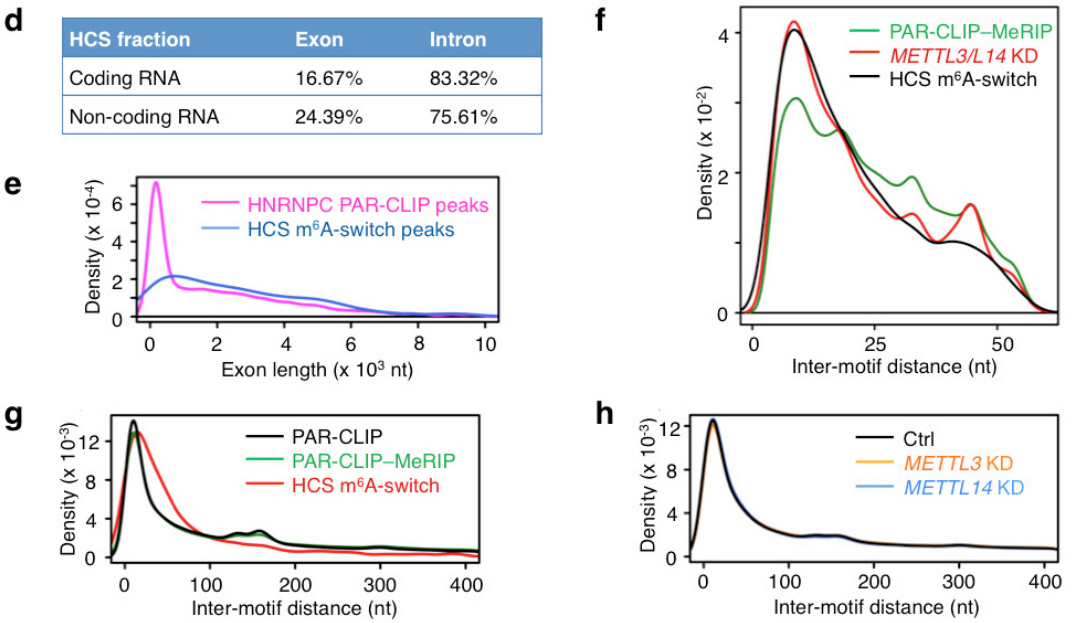

i

EVO Fraction (%)	Genome	HCS m^{6}A-switch	Fold Change
Intron	0.030	0.34	11.60
Exon	0.46	2.11	4.58
Total	0.06	0.64	10.65

Extended Data Figure 6 | Molecular features of high-confidence m^{6}A-switches. **a**, Western blot (WB) showing stable HNRNPC protein abundance upon *METTL3/L14* knockdown. **b**, Volcano plot of the *METTL3/L14* knockdown (KD) data depicting RRACH–U-tract coupling events (open red circles) as defined in Extended Data Fig. 4b, according to their *P* values[38] (*P*; *y* axis) and fold-change values at the U-tracts (*E*; *x* axis). **c**, Overlap of RRACH–U-tract coupling events with decreased HNRNPC binding by *METTL3* and *METTL14* knockdown. **d**, The intron fraction of HCS m^{6}A-switches in coding RNA and non-coding RNA. **e**, Density plot displaying the distribution of exonic m^{6}A-switches/HNRNPC PAR-CLIP peaks according to exon length. **f**, Inter-motif (RRACH–U-tract) distance distributions suggest that m^{6}A-switches have a preference for shorter distances between the RRACH and U-tract (>5×U) motifs. The distribution curves are from PAR-CLIP–MeRIP data (green), *METTL3/L14* knockdown (red) and high-confidence (HCS) m^{6}A-switches (black). **g**, Analysis of the inter-motif (U-tract–U-tract) distance patterns, previously identified by iCLIP[20], in PAR-CLIP–MeRIP, *METTL3/L14* knockdown and high-confidence m^{6}A-switch data. The peaks at ~165 and ~300 nucleotides are clearly present. For the 2,798 high-confidence switches, we analysed those in which the other U-tract motif is also in a PAR-CLIP-identified sequence; the long-range peaks seem to have shifted to longer distances (~220 and ~370 nucleotides). **h**, *METTL3/L14* knockdown does not affect the inter-motif (U-tract–U-tract) distance distributions for U-tracts (≥5× U) in HEK293T cells. **i**, EVOfold analysis for the 2,798 high-confidence m^{6}A-switches. The chances for high-confidence m^{6}A-switches to have EVOfold records are significantly higher than random genomic sequences. We first calculated the number of high-confidence sites in the EVO database if occurring in random to be ~1.7. We found that 18 high-confidence sites are present in the EVO database, resulting in ~11× enrichment. This result is further divided into intronic and exonic regions.

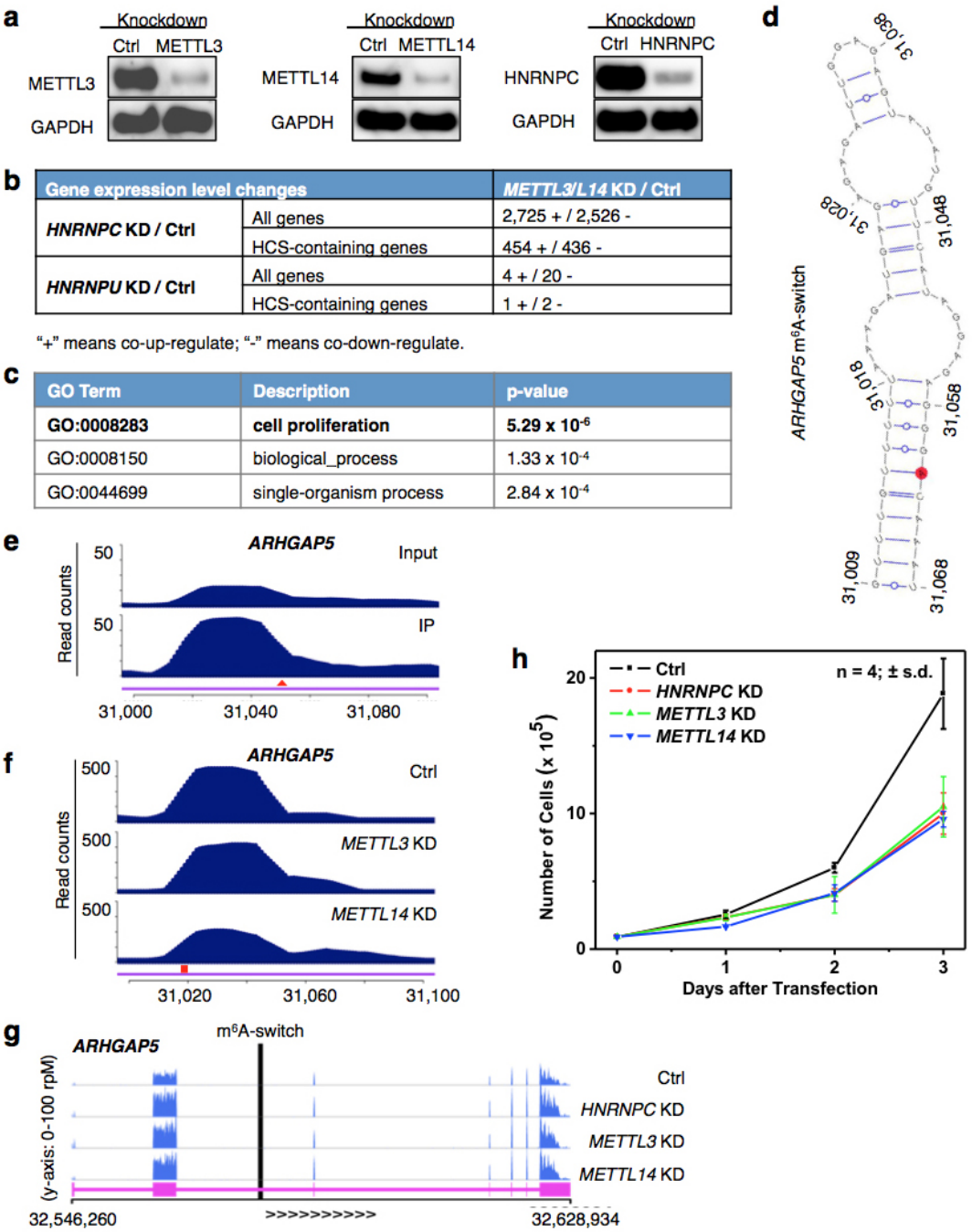

b

Gene expression level changes		METTL3/L14 KD / Ctrl
HNRNPC KD / Ctrl	All genes	2,725 + / 2,526 -
	HCS-containing genes	454 + / 436 -
HNRNPU KD / Ctrl	All genes	4 + / 20 -
	HCS-containing genes	1 + / 2 -

"+" means co-up-regulate; "-" means co-down-regulate.

c

GO Term	Description	p-value
GO:0008283	**cell proliferation**	**5.29 x 10^{-6}**
GO:0008150	biological_process	1.33 x 10^{-4}
GO:0044699	single-organism process	2.84 x 10^{-4}

Extended Data Figure 7 | m^{6}A-switches regulate the abundance of target mRNAs. **a**, *HNRNPC*, *METTL3/L14* knockdown confirmed by western blots. **b**, *HNRNPC* knockdown (KD) and *METTL3/L14* knockdown co-regulated the expression of a large number of genes. Gene expression changes between control (Ctrl) and *HNRNPC*, *HNRNPU*, *METTL3/L14* knockdown HEK293T cells were analysed by Cuffdiff2 (refs 38, 39), and the absolute numbers of differentially expressed genes are shown. HCS-containing genes refers to the 1,815 genes containing high-confidence m^{6}A-switches. The RNA-seq data from *HNRNPU* knockdown HEK293T cells (Gene Expression Omnibus accession GEO34995 data set[40]) were analysed for comparison with a different mRNA-binding protein. HNRNPU did not show preferential interaction with the 2,577–m^{6}A modified *MALAT1* hairpin (Fig. 1b, c). **c**, GO analysis of the m^{6}A-switch-containing genes whose expression levels were co-differentially regulated by *HNRNPC* and *METTL3/L14* knockdown, against all m^{6}A-switch-containing genes as background. **d**, An example of an m^{6}A-switch among co-regulated transcripts is the *ARHGAP5* transcript (NCBI accession NM_001030055). Its proposed secondary structure with the m^{6}A methylation site in red is shown with the opposing the U-tract in a stem. **e**, **f**, PAR-CLIP–MeRIP detected positive IP/input enrichment at the RRACH site (red arrowhead) of the *ARHGAP5* m^{6}A-switch (**e**), while *METTL3/L14* knockdown decreased HNRNPC binding at the U-tract (red square) of this m^{6}A-switch (**f**). **g**, The expression level of the *ARHGAP5* gene was co-upregulated by *HNRNPC*, *METTL3/L14* knockdown, as shown by the RNA-seq data from HEK293T cells. The vertical black line represents the m^{6}A-switch site. **h**, *HNRNPC*, *METTL3/L14* knockdown decreased the proliferation rates of HEK293T cells to a similar extent. Data are mean ± s.d.; $n = 4$, biological replicates.

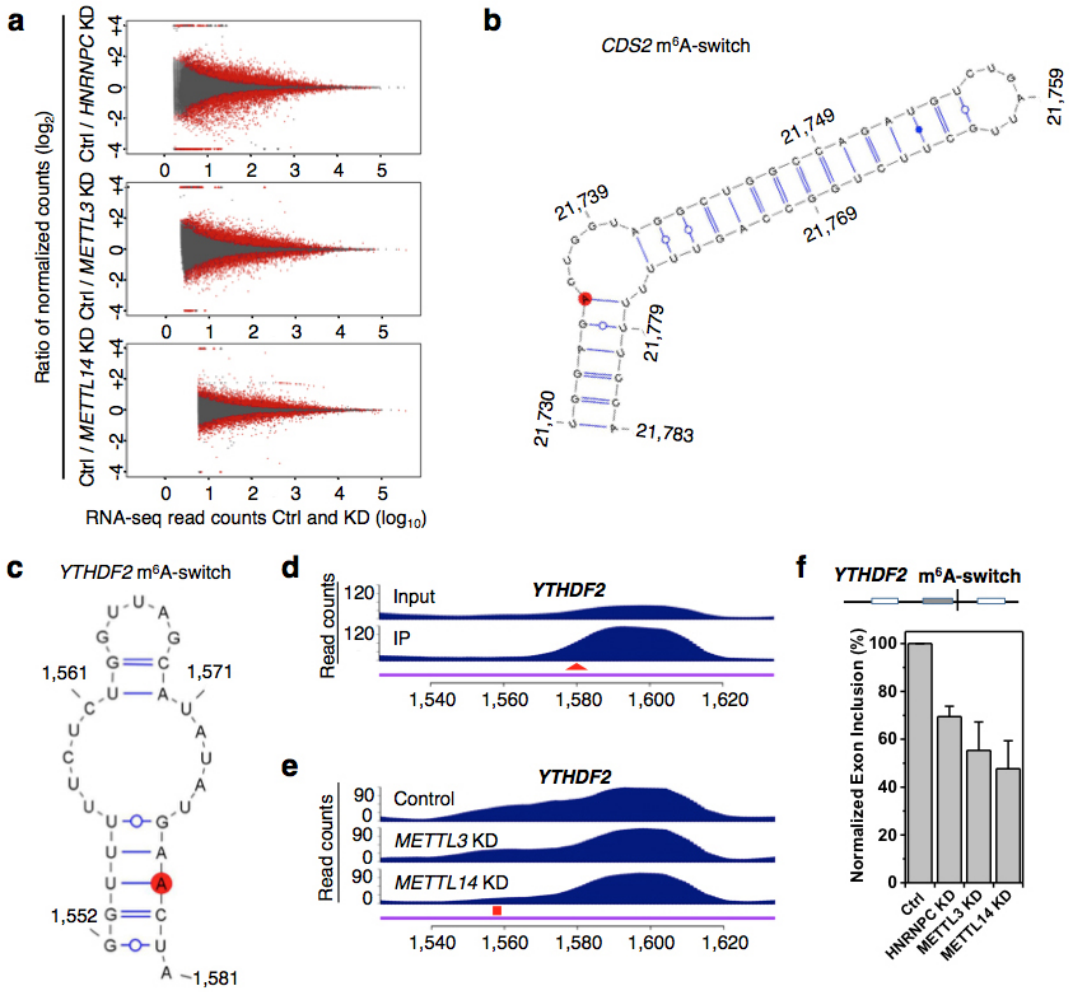

g

	Exon/Intron junction rate (reads per million)	p-value, Chi-Square test
Control	169	--
HNRNPC KD	161	1.1×10^{-15}
METTL3 KD	154	2.8×10^{-40}
METTL14 KD	156	1.6×10^{-36}

"--" meaningless in the Chi-Square test with itself.

Extended Data Figure 8 | m^{6}A-switches regulate alternative splicing of target mRNAs. **a**, Fold changes (knockdown (KD)/control (Ctrl), $\log_2$) in normalized exon expression against RNA-seq reads detect the exons in *HNRNPC* knockdown, *METTL3* knockdown, *METTL14* knockdown and control samples. Statistically significant differentially expressed exons (SSDEEs) called by DEXSeq are indicated in red. **b**, Proposed secondary structure of the *CDS2* hairpin with the m^{6}A methylation site shown in red, opposing the U-tract region. Nucleotide position numbers correspond to their locations along the human *CDS2* transcript (NCBI accession NM_003818). **c**, Proposed secondary structure of the *YTHDF2* hairpin with the m^{6}A methylation site shown in red, opposing the U-tract region. Nucleotide position numbers correspond to their locations along the human *YTHDF2* transcript (NM_001173128). **d**, **e**, PAR-CLIP–MeRIP detected a positive enrichment at the RRACH site (red arrowhead) (**d**), while *METTL3/L14* knockdown decreased HNRNPC binding at the U-tract (red square) of this *YTHDF2* m^{6}A-switch (**e**). **f**, The inclusion level of one *YTHDF2* exon is co-downregulated by *HNRNPC* knockdown, *METTL3* knockdown and *METTL14* knockdown, as validated by RT–PCR. Data are mean ± s.d.; $n = 3$, biological replicates. **g**, We analysed our polyA$^+$ RNA-seq data to look for reads that span intron/exon junctions on CDS m^{6}A-switch containing genes. We find that the control sample has significantly higher reads spanning intron/exon junctions than *HNRNPC* and *METTL3/L14* knockdown samples. This result indicates that m^{6}A depletion at the CDS m^{6}A-switches promotes intron exclusion.

a

Experiment	Sample/replicates	Mapped reads	T-to-C mutation rate
PAR-CLIP–MeRIP	Input-rep1	28,755,227	0.67
	Input-rep2	34,022,750	0.67
	IP-rep1	22,515,468	0.83
	IP-rep2	48,570,954	0.76
PAR-CLIP	Ctrl-rep1	22,728,884	0.69
	Ctrl-rep2	24,827,034	0.75
	METTL3 KD-rep1	19,697,397	0.67
	METTL3 KD-rep2	31,864,420	0.75
	METTL14 KD-rep1	20,835,499	0.67
	METTL14 KD-rep2	20,102,049	0.71

b

Experiment	Sample/replicates	Total reads	Mapped reads	Mapped rate
RNA-seq	Ctrl-rep1	78,453,301	68,058,093	86.70%
	Ctrl-rep2	78,823,710	70,907,544	90.00%
	*HNRNPC*_KD-rep1	81,933,883	72,840,271	88.90%
	*HNRNPC*_KD-rep2	78,133,137	68,053,888	87.10%
	*METTL3*_KD-rep1	58,140,943	48,123,493	82.80%
	*METTL3*_KD-rep2	58,923,206	53,011,571	90.00%
	*METTL14*_KD-rep1	77,932,017	68,703,305	88.20%
	*METTL14*_KD-rep2	75,442,883	65,812,269	87.20%

c

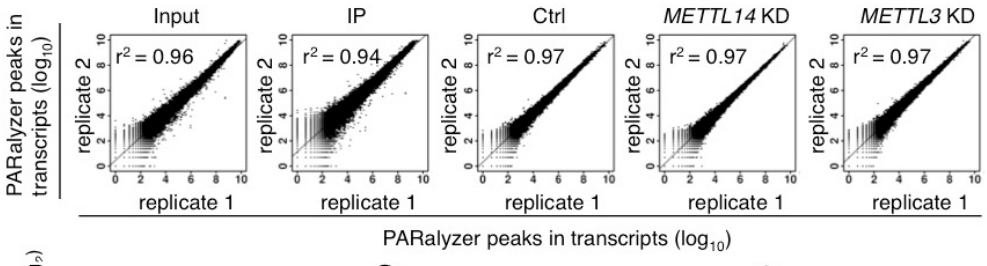

d

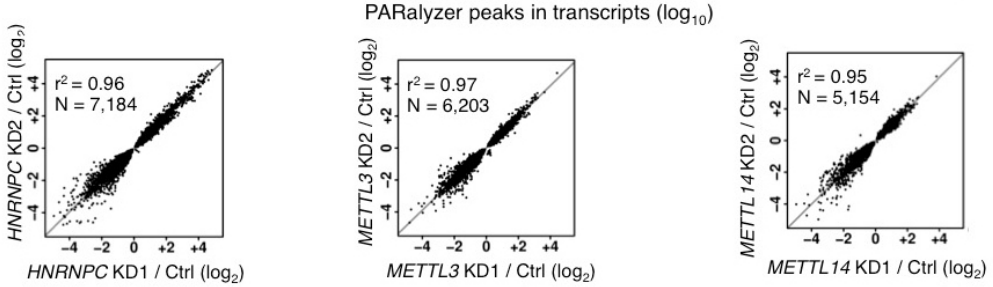

Extended Data Figure 9 | Summary of the sequencing samples. **a**, For PAR-CLIP–MeRIP and PAR-CLIP experiments from HEK293T cells, the number of mapped reads and 'T-to-C' mutation rates are given for each replicate. **b**, For RNA-seq experiments from HEK293T cells, the number of total reads, the number of mapped reads as well as the mapping rates is given for each replicate. **c**, Scatter plots comparing transcripts for all PAR-CLIP replicate experiments. The square of Spearman's rank correlation value (r^2) for each pair is shown in the top left corner of the respective panel. **d**, The detected expression level changes show a strong correlation between gene knockdown replicates. Scatter plots comparing the fold changes ($\log_2$) in normalized gene expression from replicates of *HNRNPC*, *METTL3* and *METTL14* knockdown. The square of Spearman's rank correlation value (r^2) for each pair is shown in the top left corner of the respective panel.